photonics

Review

On-Chip Lasers for Silicon Photonics

Jiangwen Zhang [1], Aadithya G. Shankar [1,2] and Xihua Wang [1,*]

1 Department of Electrical and Computer Engineering, University of Alberta, Edmonton, AB T6G 2V4, Canada; jzhang3@ualberta.ca (J.Z.); ep20b001@smail.iitm.ac.in (A.G.S.)
2 Department of Physics, Indian Institute of Technology Madras, Chennai 600036, Tamil Nadu, India
* Correspondence: xihua@ualberta.ca

Abstract: With the growing trend in the information industry, silicon photonics technology has been explored in both academia and industry and utilized for high-bandwidth data transmission. Thanks to the benefits of silicon, such as high refractive index contrast with its oxides, low loss, substantial thermal–optical effect, and compatibility with CMOS, a range of passive and active photonic devices have been demonstrated, including waveguides, modulators, photodetectors, and lasers. The most challenging aspect remains to be the on-chip laser source, whose performance is constrained by the indirect bandgap of silicon. This review paper highlights the advancements made in the field of integrated laser sources on the silicon photonics platform. These on-chip lasers are classified according to their gain media, including V semiconductors, III–V semiconductors, two-dimensional materials, and colloidal quantum dots. The methods of integrating these lasers onto silicon are also detailed in this review.

Keywords: on-chip lasers; silicon photonics; III–V materials; 2D materials; quantum dot

check for updates

Citation: Zhang, J.; Shankar, A.G.; Wang, X. On-Chip Lasers for Silicon Photonics. *Photonics* **2024**, *11*, 212. https://doi.org/10.3390/photonics11030212

Received: 26 January 2024
Revised: 23 February 2024
Accepted: 24 February 2024
Published: 27 February 2024

1. Introduction

Due to the explosive growth in global internet traffic and the demand for increased bandwidth and reduced power usage of photonic components, photonic integrated circuits (PICs) have emerged as a promising technological solution in optical communications. PICs offer unique benefits such as scalability, transparency, minimal latency, and reduced energy consumption per bit [1]. There are mainly two types of PICs: PICs based on the III–V semiconductor platform and PICs based on the silicon platform, known as silicon (Si) photonics. III–V-based PICs, which possess the characteristics of a direct bandgap and the linear electro-optic (Pockels) effect, have been brought to the commercial market in the past fifty years [2]. However, adopting pure III–V-based PICs restricts the foundry to small wafers. Specifically, these are approximately 150 mm in diameter for indium phosphide (InP) and around 200 mm for gallium arsenide (GaAs) [3]. Furthermore, small index contrast in the III–V stacks and high loss in GaAs or InP waveguides typically surpassing 1 dB/cm hampers achieving high-confinement waveguides and performance across various applications [3]. Alternatively, Si photonics emerges as a compelling choice due to the exceptional optical properties of silicon and the compatibility with the complementary metal-oxide-semiconductor (CMOS) fabrication, dominating the microelectronics. Si has exhibited numerous advantages including a high refractive index contrast with silicon dioxide, transparency within the communication wavelength range, and a notable thermo-optic coefficient for tuning [4]. Si photonics enables a broad range of applications from data communication and telecommunications to sensing, including light detection and ranging (LIDAR), gyroscopes, biosensors, and spectrometers [5]. As Si photonics has achieved commercial maturity, predicted growth rates for the associated market from 2020 to 2025 range from conservative estimates of over 20% to more optimistic estimates exceeding 30% [6].

Thanks to the benefits of Si photonics, a variety of passive and active photonic components have been successfully achieved on the integrated Si photonics platform. Several key components have been demonstrated with exceptional performance, including ultra-low loss waveguides [7–9], high-performance optical modulators [10–12], and high-speed photodetectors [13–17]. However, as an indirect bandgap material, Si restricts its light-emission efficiency. Incorporating laser sources into the Si platform to achieve on-chip lasers continues to be the greatest challenge in Si photonics technology. The prerequisites for an on-chip laser include optical power, low threshold, stability, and pumping scheme. They also require low-cost and high-volume production. Currently, researchers are exploring various materials and integration methods to develop high-performance on-chip lasers.

Certain seminal reviews have summarized the history, recent progress, and perspective trends of the on-chip light sources [18,19]. In this paper, we conduct a more comprehensive review, focusing specifically on the recent advances in on-chip lasers with different materials utilizing different integration technologies. In Section 2, we will discuss Group IV semiconductors based on-chip lasers, including Ge-on-Si lasers and enhanced GeSn lasers. Both lasers leverage the epitaxial growth of Ge on Si. Section 3 will concentrate on III–V-material-based on-chip lasers. We will introduce the existing four methods for integrating III–V materials on Si substrates, including flip-chip integration, heterogeneous integration, monolithic integration, and transfer printing techniques. In Section 4, we will introduce on-chip lasers based on two-dimensional materials (2DMs) as optical gain materials. For achieving on-chip lasing, the most efficient strategy is to construct optical nanocavities combined with 2DMs. Photonic crystal cavity-based nanolasers and microdisk cavity-based nanolasers will be included. Lastly, in Section 5, we will explore the advancements in wavelength-tunable colloidal quantum dot (CQD) lasers and underscore their potential for integration with silicon-based optical components.

2. Group-IV-Material-Based Lasers

Group IV materials are not considered ideal candidates for lasers since they typically have indirect bandgaps and are unsuitable for lasing. However, progress has been made in demonstrating Ge and GeSn lasers using the monolithic integration technique [20,21]. The epitaxial growth of Ge on Si offers an exciting approach for integrated lasers. Pure Ge and Si have significant lattice mismatches and distinct thermal expansion coefficients [22]. Although Ge does have an indirect bandgap structure, the energy gap (0.8 eV) from the top of the valence band to the momentum-aligned Γ valley is close to the actual bandgap (0.66 eV). In addition, the larger thermal expansion coefficient of Ge leaves a thermal strain in Ge after growth on Si. The strain reduces the energy difference between the Γ and L valley to 115 meV [23]. When heavily n-doped, the free electrons fill up the L valley to a level equal to that of the Γ valley, which increases the probability of radiative recombination between the Γ valley and the valence band. Such a feature has enabled CW room-temperature optically pumped Ge-on-Si lasers [24]. However, these lasers have extremely high lasing threshold current density [25]. The drawbacks of indirect bandgap Ge can be overcome by introducing high tensile strain, resulting in increased material gain [26]. Another approach is to alloy tin (Se) into Ge with a reasonably high Sn concentration (>6.5%) to achieve direct bandgap. Lasing from GeSn alloys and GeSn/SiGeSn heterostructures has been observed [27]. In this section, we will discuss the progress made in Ge-on-Si lasers and GeSn/SiGeSn-based lasers.

2.1. Ge-on-Si Lasers

Liu et al. reported the first observation of lasing from the direct bandgap transition of Ge-on-Si at room temperature [25]. A thermally induced tensile strain of 0.24% and phosphorus doping of 1×10^9 cm^{-3} shrank the direct gap of Ge to 0.76 eV, allowing enhanced light emission. The device was fabricated by the epitaxial growth of 1.6 µm × 0.5 µm Ge waveguides on Si, whose edges were mirror-polished. The length of the waveguides was 4.8 mm, forming a mirror-polished Fabry–Pérot cavity. The cavity was excited by a 1064 nm

Q-switched laser with a pulse duration of 1.5 ns. The peak pump power density absorbed by the Ge was estimated to be 300 kW cm^{-2}. A broad photoluminescence peak at 1600 nm was observed when pumped at 1.5 μJ per pulse. Emission peaks at 1599, 1606 and 1612 nm emerged. When the pump increases to 6.0 μJ per pulse, a shoulder is visible at 1594 nm, which corresponds to the lasing threshold in the inset of Figure 1a.

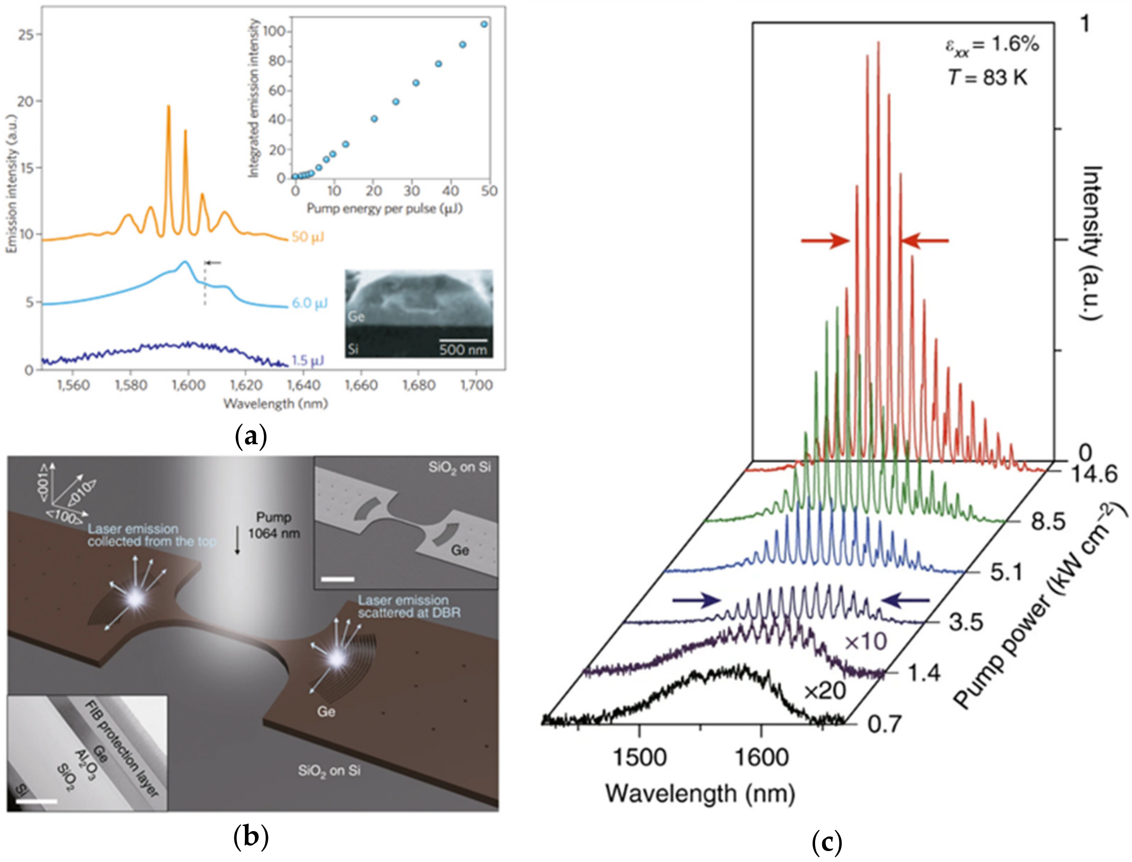

Figure 1. (**a**) Edge-emission spectra of a Fabry–Pérot Ge waveguide under three different levels of optical pumping from a Q-switched laser at 1064 nm with a pulse duration of 1.5 ns and at a repetition rate of 1 kHz is shown. Top inset: integral emission intensity from the waveguide facet versus optical pump power, showing the lasing threshold. Bottom inset: cross-sectional SEM image of the Ge waveguide [25]. Reproduced with permission from Nature Photonics; published by Springer Nature, 2010. (**b**) Schematic of the Ge nanowire laser consisting of a strained nanowire surrounded by a pair of distributed Bragg reflectors (DBRs) [28]. Reproduced with permission from Nature Communications; published by Springer Nature, 2017. (**c**) Power-dependent photoluminescence spectra of a 1.6%-strained Ge nanowire with distributed Bragg reflectors (DBRs). The first and second spectra are multiplied by a factor of 20 and 10, respectively, for clarity. The arrows indicate an emission bandwidth of ~150 nm near the threshold (blue) and of <50 nm in the lasing regime (red) [28]. Reproduced with permission from Nature Communications; published by Springer Nature, 2017.

In 2017, a low-threshold Group IV laser employing a Ge nanowire with a 1.6% uniaxial tensile strain integrated with distributed Bragg reflectors, as shown in Figure 1b, was demonstrated [28]. Multimode lasing at a low temperature of 83 K was observed. The emission spectra at different pump powers are shown in Figure 1c. At a pump power of 3.5 kW cm^{-2}, a significant reduction in linewidth was observed along with an increase in the intensity of cavity modes, owing to the presence of DBRs, near the band edge. The full-width at half-maximum of the emission band is ~150 nm with a node spacing of ~8 nm.

2.2. GeSn Lasers

Another approach to making integrated lasers from Group IV materials is through GeSn semiconductors [27,29–31]. When Sn content is more than 9%, GeSn turns into a direct bandgap material [32], a crucial requirement for efficient light emission. Furthermore, GeSn epitaxy is monolithic on Si [33] and compatible with CMOS technology, making it a promising candidate for realizing integrated lasers on Si.

The first GeSn laser was reported by Wirths et al. in 2015 [32]. They presented a laser with 12.6% Sn operating up to 90 K. Subsequently, it was shown that 20% Sn incorporation led to room-temperature laser operation [29]. A lower threshold was achieved by employing SiGeSn/GeSn heterostructures. Stange et al. demonstrated lasing in GeSn multi-quantum-well heterostructures with SiGeSn barriers [27], as shown in Figure 2a. The concentration of Sn in the active layers was ~13% and reported a lasing threshold of 40 kW/cm^{-2} at 20 K, as shown in Figure 2b. In 2020, Elbaz et al. reported a continuous-wave optically pumped laser with a Sn composition as low as 5.4% in a tensile-strained disk structure [31]. They transformed the indirect-bandgap semiconductor, a 300 nm GeSn layer with 5.4% Sn, to a direct-bandgap semiconductor by tensile straining through a SiNx stressor layer. Figure 2c shows the SEM images of the under-etched GeSn/SiNx stack and the final laser structure with SiNx. They observed continuous-wave and pulsed lasing at 70 K and 100 K, respectively. At an operation wavelength of 2.5 µm, thresholds of 1.1 kW cm^{-2} and 0.8 kW cm^{-2} were achieved under continuous-wave and nanosecond pulsed optical excitation, respectively. The first electrically injected GeSn diode laser was demonstrated by Zhou et al. [34]. They employed a GeSn/SiGeSn double heterostructure to ensure carrier and optical confinement. Pulsed lasing up to 100 K was observed for the ridge waveguide GeSn laser, with a peak wavelength of 2300 nm. A threshold of 598 A/cm^2 and peak power of 2.7 mW/facet was measured at 10 K.

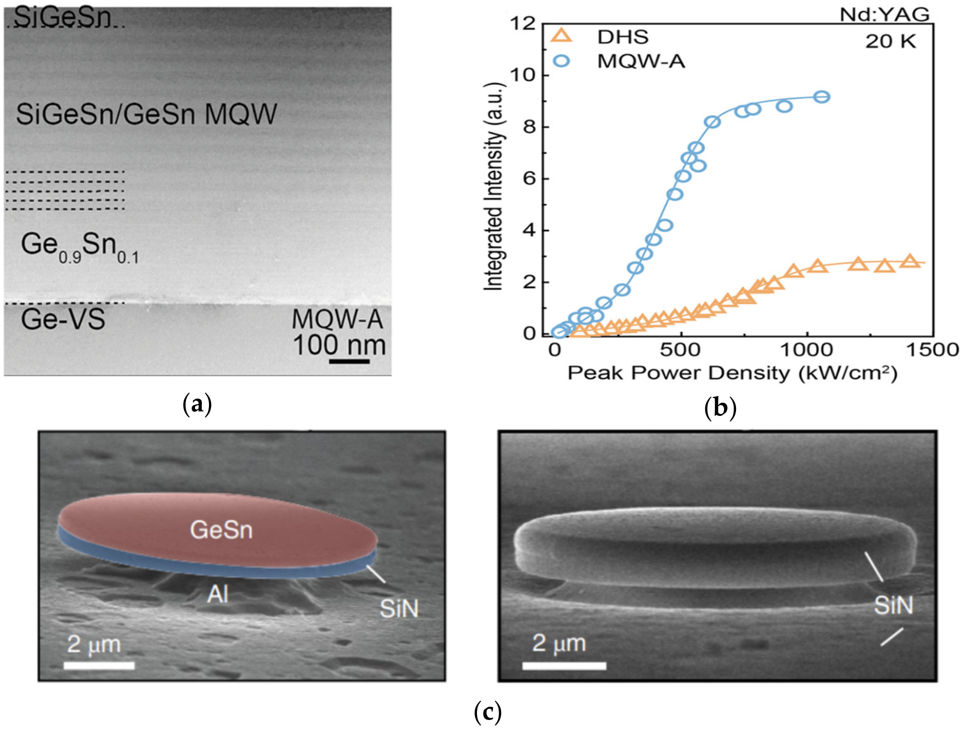

Figure 2. (**a**) X-TEM image of a multi-quantum well [27]. Reproduced with permission from ACS Photonics; published by American Chemical Society, 2018. (**b**) 20 K integrated intensity vs. peak power densities for multi-quantum-well and double-heterostructure lasers [27]. Reproduced with permission from ACS Photonics; published by American Chemical Society, 2018. (**c**) SEM images of the under-etched GeSn/SiNx stack and the final laser structure with SiNx [31]. Reproduced with permission from Nature Photonics; published by Springer Nature, 2020.

3. III–V-Material-Based Lasers

Si, being an indirect bandgap semiconductor, is a poor emitter of light. This limitation can be overcome by integrating III–V materials, such as GaAs and InP, on Si. By doing so, the high carrier mobility and bandgap engineering potential of III–V can be exploited to realize lasers on Si substrates. In this field, several noteworthy reviews were published in the past [35–38]. Here, we conduct the review based on the methods for integrating III–V materials on Si substrates [39,40], including flip-chip integration [41,42], heterogeneous integration, monolithic integration, and transfer printing techniques [43,44].

3.1. Heterogeneous Integration

In heterogeneous integration, well-established III–V light-emitting sources are fabricated onto Si substrates. The transfer is done through a variety of physical/chemical bonding methods. Heterogeneous integration has high tolerance in lattice mismatches, couples high-efficiency III–V light sources with high-caliber Si passive waveguide components, and requires no severe positioning alignment. An accurate alignment between III–V lasers and silicon waveguides is the key to success, and the integration density is determined by the pitch density and the size of the bumps [45]. By utilizing high-precision lithography to process III–V thin films and align III–V devices with wafer-level silicon-on-insulator (SOI) circuits, one can realize a high density of integration at a lower cost. There exists a variety of bonding techniques such as anodic bonding, solder bonding [46], thermocompression bonding [47], ultrasonic bonding [48], eutectic bonding [49], adhesive bonding, direct metal–metal bonding, low-temperature melting-glass bonding [50], and dies-to-wafer (D2W) bonding [51]. Here, we will focus on D2W bonding and adhesive bonding.

3.1.1. D2W Bonding

D2W bonding enables seamless integration of laser sources and Si photonic circuits and has high integration potential. High-throughput III–V laser integration on Si was reported in [52] and has since been used to realize tunable microring lasers bonded on Si. Here, a Si metal-oxide-semiconductor (MOS) capacitor is integrated into the laser cavity. The addition of the MOS capacitor introduced the plasma-dispersion effect, which can change the laser mode refractive index and cavity loss, allowing the lasing wavelength and output power to be tuned. The device's schematic is illustrated in Figure 3a. As shown in Figure 3a, the laser has an InP microring resonator coupled with a Si bus waveguide. The MOS capacitor is formed by a dielectric layer sandwiched between n-InP and the Si waveguide. The laser is fabricated by bonding III–V to patterned Si and then patterning the III–V sample. As shown in the transmission electron microscopy (TEM) image (Figure 3d), the oxide dielectric layer has a thickness of 18 nm. The layer is formed as the byproduct of the low-temperature O_2 plasma-assisted bonding process. From Figure 3b, we can see that the optical mode overlaps with the capacitor region. Hence, by applying a bias voltage, we can modify the effective index and free carrier absorption loss. As shown in Figure 3c, the MOS capacitor's bias voltage affects the lasing wavelength and photocurrent. Hence, it functions as a highly efficient tunable laser.

An advanced heterogeneous scheme that combines the advantages of monolithic integration with major dislocation origins was demonstrated by Fujii et al. [53]. The approach was on a multi-quantum-well (MQW) active region integrated on a Si wafer by bonding. InGaAs/AlGaAs QW lasers have also been demonstrated on a Si substrate, adopting a three-step-grown thin and simple buffer layer, resulting in a reduced threading dislocation density and interface roughness and achieving a low-threshold current density [54]. InP-based quantum-well lasers have also been demonstrated at 2.3 μm [55] and 1.55 μm [56]. Quantum-dot (QD) lasers are preferred over quantum-well lasers because they have a greater laser thermal stability and lower lasing threshold due to 3D confinement of the carriers. A theoretical framework for heterogeneous integration of QD lasers on Si can be found in [57,58]. Quantum-dot lasers bonded on Si have been reported recently. A single-mode InAs/GaAs quantum-dot distributed feedback (DFB) laser bonded on Si was reported in

2018 [59]. A high-temperature operation with a continuous-wave operation up to 100 °C and a current density as low as 205 A/cm^2 were obtained. The authors achieved single-mode lasing at 1300 nm with side-mode suppression of 40 dB. In 2021, record evanescent QD-distributed feedback lasers on Si were reported [60]. The laser had a 3 dB modulation bandwidth of 13 GHz, a threshold current of 4 mA, a side-mode-suppression ratio of 60 dB, and a fundamental linewidth of 26 kHz. Significant improvements in the thermal stability of QD lasers were achieved in 2023 via heterogeneous integration on silicon carbide (SiC) substrates [61]. A relatively temperature-insensitive operation near room temperature and lasing up to 105 °C was reported.

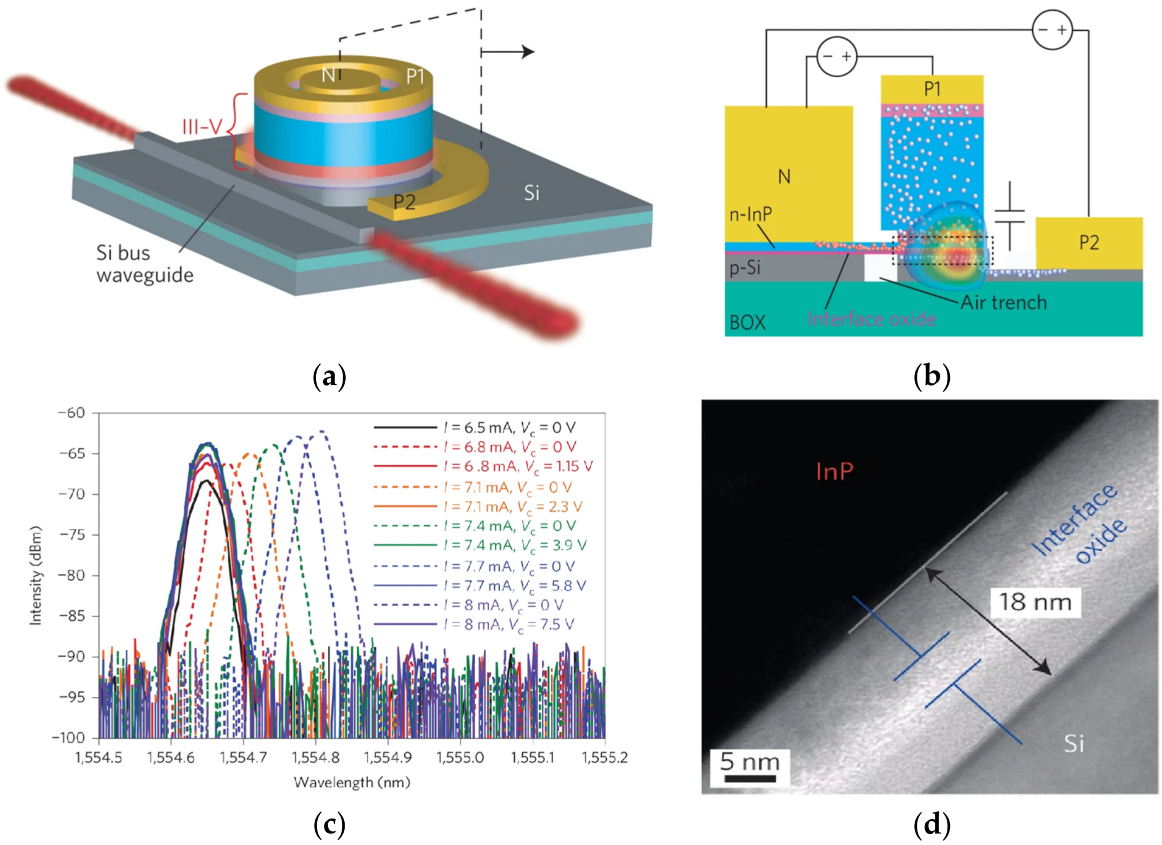

Figure 3. (**a**) 3D schematic of the laser. (**b**) Cross-sectional view of the laser including MOS capacitor and optical mode. (**c**) Device wavelength redshift from injection current heating (dashed lines) and locking (solid lines) by an appropriate MOS bias Vc. (**d**) TEM image of the oxide dielectric layer sandwiched between the InP layer and Si layer, forming an MOS capacitor for laser fine-tuning. Reference [52]. Reproduced with permission from Nature Photonics; published by Springer Nature, 2016.

In 2020, Xiang et al. [62] reported a low-phase-noise, high-temperature-stable III-V/Si/Si_3N_4 heterogeneously bonded laser. They overcame the large refractive index mismatch between Si_3N_4 and III–V materials by using multilayer heterogeneous integration that employs multiple mode transitions. The III–V/Si hybrid waveguide transitions to a Si waveguide through a Si/Si_3N_4 transition to the SiN waveguide. The multilayer heterogeneous integration is shown in Figure 4a. As shown, first the Si_3N_4 passive layer is deposited and processed. Subsequently, the Si layer and III–V epitaxial layer are transferred to the Si_3N_4 waveguides via wafer bonding. The schematic of the laser is shown in Figure 4b. The lasing-wavelength shift under temperature variation was reported to be 10.46 pm/C for the III–V/Si/SiN laser (Figure 4c). This is lower than that of a III–V/Si laser, whose value is reported as 73.18 pm/C (Figure 4c). The white-noise-limited frequency noise level of the III–V/Si/Si_3N_4 laser was reported to be 1300 Hz^2/Hz, while its Lorentzian linewidth was 4 kHz. The superior performance of the laser is attributed to the low loss and low thermal sensitivity of the Si_3N_4 waveguide.

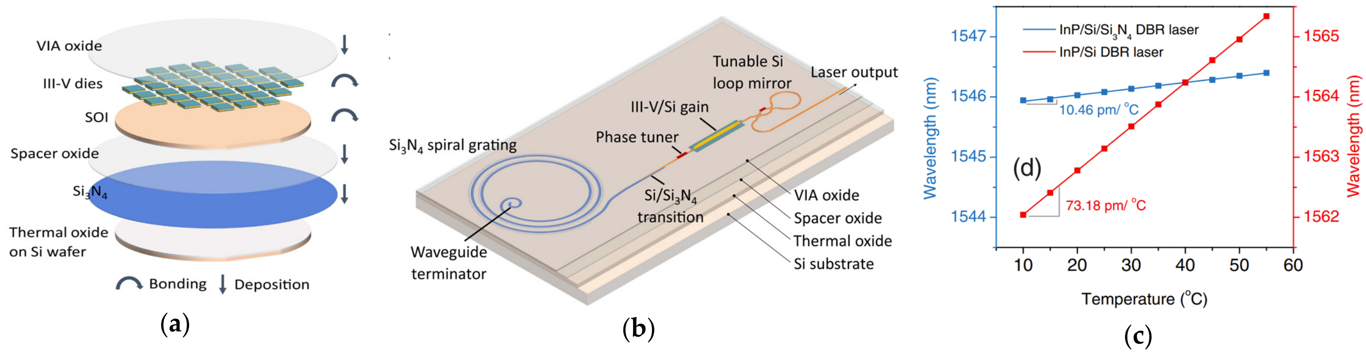

Figure 4. (**a**) Schematic of multilayer heterogeneous integration. (**b**) Schematic of the III–V/Si/Si_3N_4 laser. (**c**) Lasing-wavelength dependence on stage temperature. Reprinted with permission from [62] © Optical Society of America.

In 2020, a turnkey operational regime for the co-integration of soliton microcombs with a pump laser was achieved [63]. Rizzo et al. showcased a highly scalable silicon photonic data communication link, employing a Kerr comb source [64]. This system operates at a state-of-the-art aggregate bandwidth, facilitated by massively parallel dense wavelength-division multiplexing. In 2021, a significant milestone in heterogeneous integration techniques was achieved, wherein the first demonstration of a heterogeneously integrated soliton microcomb combining an InP/Si laser and ultralow-loss Si_3N_4 microresonator on a monolithic Si substrate was made [65]. Important achievements were also realized in silicon nitride photonics. A high-performance laser on SiN with tens of milliwatts output power and a sub-kHz fundamental linewidth was reported in 2021 [66]. In 2022, the three-dimensional integration of III–V gain medium and low-loss silicon nitride waveguides resulted in an ultralow-noise laser with isolator-free operation [67].

3.1.2. Adhesive Bonding

Adhesive bonding employs polymer adhesives such as epoxies, polyimides, resists, spin-on-glass, and divinylsiloxane-bis-benzocyclobutene (DVS-BCB) as an intermediate layer for bonding to increase bonding strength. Usage of DVS-BCB as the adhesive results in high bonding strength and the formation of void-free bonds due to low-volume shrinkage of the adhesive [68]. In adhesive bonding, a thin layer of the adhesive is applied to one of the two mating wafers followed by ultraviolet light pre-curing, room-temperature pre-bonding, and low-temperature annealing. As the adhesive bonding process does not require high temperature, it reduces the risk of III–V layer damage [69].

Roelkens et al. showed the indium gallium arsenide phosphide (InGaAsP) quantum-well (QW) laser and photodetector bonding on a Si substrate via DVS-BCB [45]. By introducing an inverted adiabatic taper from a Si waveguide to the III–V mesa, they increased the coupling efficiency. In 2017, a III–V on Si comb laser based on DVS-BCB adhesive bonding was demonstrated [70]. The comb laser, as shown in Figure 5a, consists of a III–V laser integrated with a 400 nm thick SOI wafer with a 30 nm thick DVS-BCB adhesive bonding layer. A 37.4 mm low-loss Si waveguide acts as the laser cavity and enables the laser to be locked at a repetition rate of 1 GHz, and the optical comb consists of more than 1400 phase-locked lines, as shown in Figure 5b.

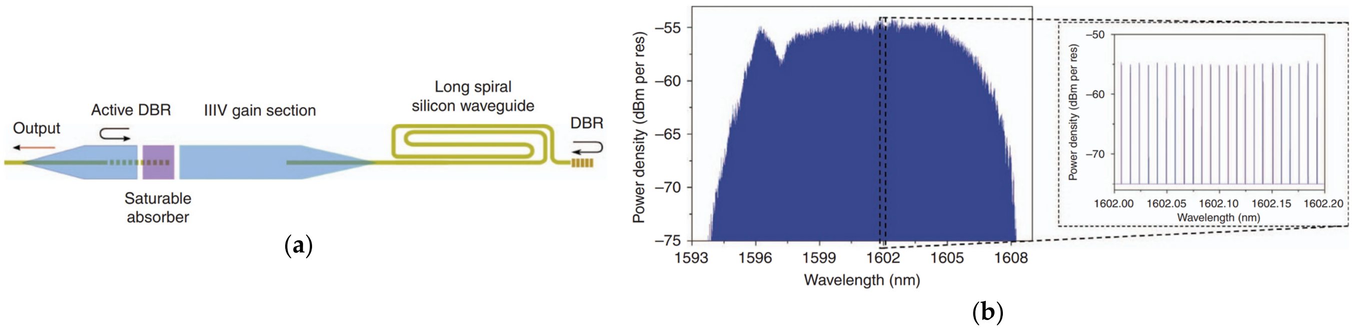

Figure 5. (**a**) Schematic of the laser. (**b**) Optical comb generated by the passively locked 1 GHz MLL. Inset: a detail of evenly spaced optical modes in the comb. Reference [70]. Reproduced with permission from Light: Science & Applications; published by Springer Nature, 2016.

3.2. Monolithic Integration

In monolithic integration, III–V lasers are integrated on Si by growing III–V semiconductor compounds epitaxially on Si. Monolithic integration achieves lower manufacturing costs by using cheaper substrates and is scalable [40,71]. However, it is challenging to overcome the crystalline lattice mismatch, anti-phase domains, and thermal cracks due to differences in physical properties between III–V and Group IV materials [71,72]. The lattice mismatch contributes to the formation of threaded dislocations which degrades laser performance by creating non-radiative recombination centers [71]. Furthermore, the mismatch in the thermal expansion coefficient causes cracks in the material when cooling from high temperature. The first double-heterostructure GaAs/AlGaAs grown on Si working at 77 K was demonstrated by Windhorn et al. in 1984 [73]. A year later, room-temperature operation was achieved [74]. Subsequently, a large number of studies on single quantum-well and multiple quantum-well lasers were carried out. Fischer et al. demonstrated an AlGaAs/GaAs single QW laser with a threshold current of 6.9 kA/cm^2 at 7 °C [75]. The first telecommunication-wavelength multiple QW laser was demonstrated by Razeghi et al. at 1.3 µm [76,77]. The demonstration of 1.3 um lasers meant that the laser on Si could be used as a telecommunication and inter-chip connection. Hu et al. demonstrated a novel photonic integration method of the epitaxial regrowth of III/V on a III/V on an SOI bonding template [40]. The grown MQW structure showed a significantly low dislocation density of 9.5×10^4 cm^{-2}. The laser showed room-temperature CW and pulsed lasing at 1.31 µm with a minimal threshold current density of 813 A/cm^2. In 2022, an advanced integration scheme of AlGaIn-based laser sources on Si was demonstrated by bonding a thin InP seed on which further regrowth steps were implemented [78]. The AlGaInAs-based MQW laser was grown onto InP-SiO_2/Si. The structure demonstrated laser performance was similar to the ones obtained by growing the structure on InP. The regrowth on InP-SOI wafers holds promise to combine the best from the III–V monolithic platform with Si photonics circuitry. Egawa et al. grew the first quantum-dot laser on Si [79]. Quantum-dot lasers are preferred over QW lasers due to their low-threshold current and high-temperature performance due to their delta-function-like density of states. Quantum-dot lasers also have a strong tolerance to threading dislocations, due to which they exhibit better performance [80].

In 2015, Wang et al. demonstrated an optically pumped DFB laser via the selective growth of III–V material [72]. The laser schematic is shown in Figure 6a. The DFB cavity is formed by an InP waveguide with gratings. Figure 6b shows the emission spectra under different pumping conditions. The lasing peak is obtained at 930.5 nm with a side-mode-suppression ratio (SMSR) > 20 dB. A 65% reduction in lasing threshold was observed when InGaAs was used as the gain medium instead of InP [7]. In 2017, Norman et al. demonstrated an electrically injected Fabry–Pérot quantum-dot laser grown on on-axis (001) Si patterned with {111} v-grooves lying along the [110] direction [81]. Such an approach circumvents the issue of anti-phase domains and reduces the dislocation density. By employing a GaAs-on-v-groove-silicon (GoVS) approach, they demonstrated continuous-wave (CW) wave operation up to 80 °C with threshold currents as low as 37 mA. A similar v-groove approach was taken by Wei et al. to grow an InAs/GaAs quantum-dot laser on an SOI substrate [82]. The DM laser provided stable single-mode operation with a threshold current of 45 mA and output power of 9 mW.

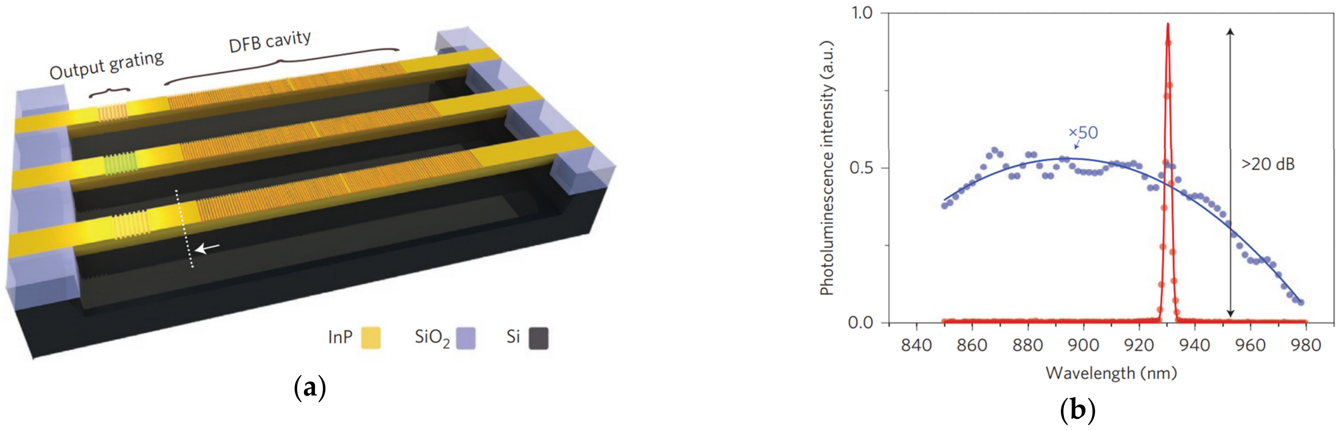

Figure 6. (**a**) 3D schematic of a monolithically integrated DFB laser on Si. (**b**) Room-temperature laser emission spectra measured below (blue) and above (red) the threshold. Reference [72]. Reproduced with permission from Nature Photonics; published by Springer Nature, 2015.

In 2016, Chen et al. demonstrated a high-performance CW InAs/GaAs quantum-dot laser [80]. The InAs/GaAs quantum-dot lasers were directly grown on a Si substrate using molecular beam epitaxy (MBE). The laser operated with a low-threshold current density of 62.5 A/cm^2, an output power greater than 105 mW at room temperature, and gave stable output up to 120 °C. The mean time to failure was extrapolated to be over 100,158 h. The high performance of the laser is due to the achievement of the low density of threading dislocations (10^5 cm^{-2}) in the III–V epilayers. This was achieved by combining a thin nucleation layer of AlAs and a dislocation filter layer with in situ thermal annealing. Further, Wan et al. demonstrated the first 1.3 µm room-temperature continuous-wave InAs QD microdisk laser grown epitaxially on Si (001) substrates [83]. This was followed by the realization of subwavelength microdisk lasers as small as 1 µm [84] and 1.3 µm submilliamp threshold QD lasers grown epitaxially on Si (001) [85]. Jung et al. in 2018 achieved a wall-plug efficiency of 38.4% at a low-threshold current of 9.5 mA in 1.3 µm InAs QD lasers on on-axis (001) GaP/Si [86]. In 2019, Kwoen et al. reported a high-temperature (100 °C) CW operation of an InAs/GaAs quantum-dot laser directly grown on an on-axis Si (001) substrate through MBE [87]. The threshold current density at room temperature was as low as 370 A/cm^2 and CW operation was observed up to 101 °C in the device. Tunable QD lasers directly grown on Si were demonstrated in 2019 as well [88]. This was followed by tunable InAs/GaAs QD lasers at 1.3 µm [89] and QD DFB on Si (001) [90]. Wan et al., in 2020, demonstrated a CW InAs/GaAs QD laser directly grown on quasinominal Si (001) substrates with a 0.4° offcut angle [91]. They achieved lasing at 1.3 µm and a maximum operating temperature of 80 °C. A novel asymmetric step-graded filter structure achieved a threading dislocation density lower than 2×10^6 cm^{-2}, providing a pathway to reach the theoretical limit of the order 10^5 cm^{-2} [92]. This was subsequently exploited to show record-breaking reliability of InAs QD lasers on Si (001) at 80 °C [93]. In 2022, Shang et al. demonstrated the first electrically pumped quantum-dot laser grown on a 300 mm patterned (001) Si wafer [94]. The laser was grown by MBE and emitted around 1300 nm. The maximum double-sided output power of 126.6 mW was achieved at 20 °C. The highest double-side wall-plug efficiency of 8.6% was achieved at an injection current of 214 mA, while the threshold current was 47.5 mA. Wei et al. demonstrated an InAs/GaAs quantum-dot laser on a trenched SOI substrate [95]. Figure 7a shows the schematic of the III–V quantum dot laser on SOI substrate. The device consists of an 8-inch SOI wafer with pre-patterned laser tranches and Si waveguides, as shown in Figure 7b. Inside the laser trench, periodic silicon grating structures are patterned. The grating structures cover the entire laser trench for high-quality III–V direct epitaxial growth. The III–V laser on SOI achieved CW lasing up to 85 °C with a maximum output power of 6.8 mW. Reflection insensitivity holds paramount importance for PIC applications, where external reflections can swiftly accumulate from various internal interfaces, potentially disrupting the laser source. The isolator-free Si-integrated III–V quantum-dot laser source eliminates the need for such isolators, while still maintaining the required feedback tolerance. Research on the feedback insensitivity of III–V quantum-dot lasers epitaxially grown on a Si substrate has been conducted. The findings indicate that III–V quantum-dot lasers on Si demonstrate a stronger feedback tolerance compared to quantum-well lasers [96,97].

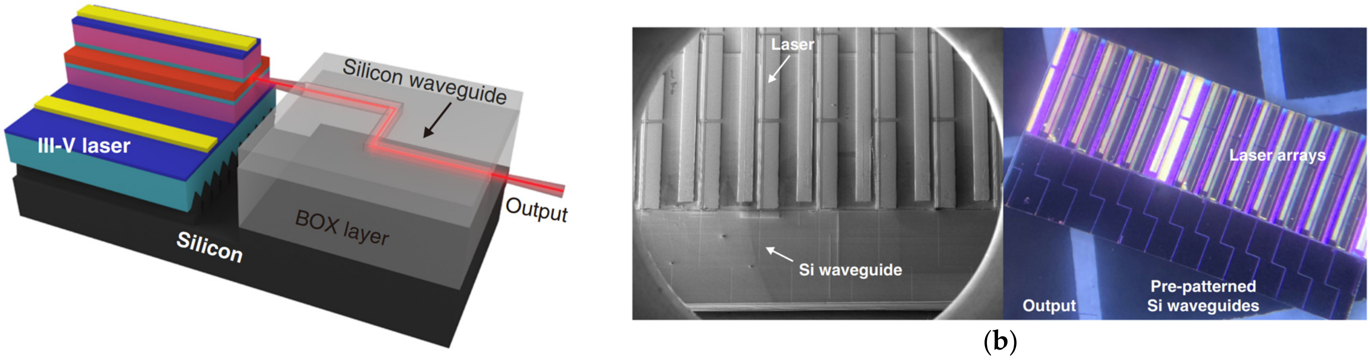

(a) (b)

Figure 7. (**a**) Schematic of the monolithic integration of a III–V quantum dot laser coupled with a silicon waveguide on an SOI platform. (**b**) Left: SEM image of the InAs quantum-dot laser array grown in pre-patterned laser trenches. Right: Optical microscope image of the entire chip. Reference [95]. Reproduced with permission from Light: Science & Applications; published by Springer Nature, 2023.

Another important class of III–V-material-based lasers is III-Nitride (III-N) lasers. These are primarily used to realize devices on Si that emit at blue wavelengths. A detailed review of III-N semiconductor lasers grown on Si is presented in [98]. Recently, in 2020, a low-loss photonic integrated circuit platform at blue wavelength was reported [99]. A coupling efficiency of 74% was achieved between the SiN waveguide and GaN laser diode at a wavelength of 450 nm. A low-phase-noise hybrid integrated laser comprising a GaN-based laser diode and SiN photonic chip-based microresonator operated at wavelengths as low as 410 nm [100]. The low phase noise was achieved via self-injection locking of the Fabry–Pérot diode laser to a high-Q photonic integrated microresonator. This was followed by the demonstration of low-phase-noise, narrow emission linewidth integrated photonic laser diodes at 412 nm and 461 nm [101,102].

4. 2D-Material-Based Lasers

Two-dimensional (2D) materials have been extensively researched recently. Graphane [103], transition metal dichalcogenides (TMDCs) [104], and black phosphorus [105] have been demonstrated for photodetection. Low manufacturing costs and easy integration with silicon further also enhance the suitability of 2D materials as potential candidates for on-chip light sources. The quantum confinement effect gives 2D materials unique optical properties, making them ideal candidates for applications in light-emission devices. The stacking of individual atomic planes through the van der Waals force enables the simple exfoliation of 2D materials from bulk materials, which can be transferred onto an integrated silicon chip without the need for any adhesives [106]. However, the lack of bandgap and the weak light-absorption properties of graphene limit its application in optoelectronics [107].

TMDCs have stood out as gain materials due to their physical and chemical properties, including high exciton-binding energy [108], long-lived population inversion [109], and broadband absorption [107]. The main challenge of developing 2D-material-based nanolasers is due to the low quantum yield caused by crystal defects [110], exciton–exciton annihilation [111], and Auger recombination [112]. To achieve on-chip lasing, the most effective approach is to design optical nanocavities with a high Q factor to enhance the Purcell effect [113].

4.1. Photonic Crystal Cavity-Based Nanolasers

In 2017, Li et al. first reported a silicon photonic crystal nanobeam cavity laser integrated with a monolayer of $MoTe_2$ operated in the near-infrared range at room temperature [114]. Figure 8a demonstrates the structure of the device, which includes a 1D photonic bandgap with periodic air holes within a silicon waveguide and two "mirror" segments. The high Q factor of 5603 was achieved by the ability to sustain high-quality optical resonance. When pumped by the CW laser at room temperature, this laser exhibited lasing at 1132 nm with a narrow linewidth of 0.202 nm. Fang et al. reported a silicon-laser-like emission using multilayer $MoTe_2$ as the gain material within a silicon photonic crystal L3 nanocavity with a Q factor of 2660 (Figure 8b) [115]. The study demonstrates optically pumped $MoTe_2$-on-silicon lasing at 1305 nm, achieved at room temperature with a threshold power density of 1.5 kW/cm^2. The utilization of multilayer $MoTe_2$ provides a greater degree of overlap between the 2D gain material and the optical mode, ensuring an adequate gain. In addition to monolayer TMDCs, heterobilayers consisting of MoS_2 and WSe_2 can also be employed to make a laser [113]. In this structure, the relaxation of photoinduced electrons takes place from the higher-level conduction band to the lower-level conduction band (Figure 8c). This phenomenon is driven by the energy difference between the conduction bands of the two different 2DMs. Consequently, photons with lower energy are emitted compared to the intralayer excitons of both WSe_2 and $MoSe_2$. Liu et al. reported a room-temperature laser with MoS_2/WSe_2 heterostructures integrated on an L3-type Si photonic crystal cavity (PhCC) [116]. The PhCC design (Figure 8d) employed in this study enabled the effective funneling of spontaneous emissions from the Van der Waals gain material into the cavity mode, leading to efficient photon confinement. The lasing device demonstrated in this study operated at 1128.6 nm and exhibited an ultra-low threshold of approximately 54 μW at room temperature.

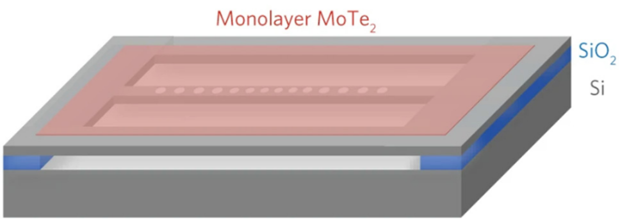

(**a**)

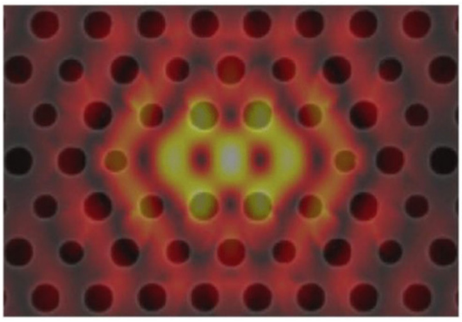

(**b**)

Figure 8. *Cont.*

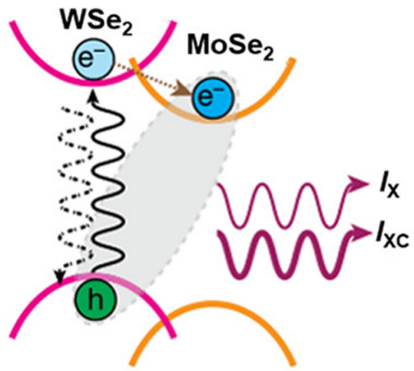

(**c**)

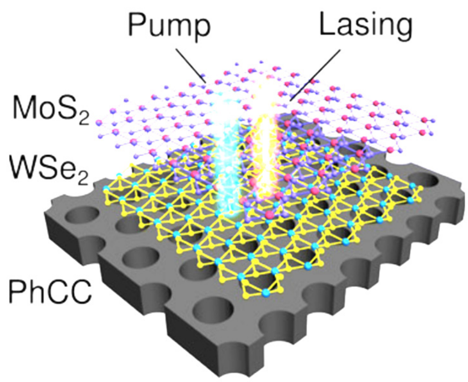

(**d**)

Figure 8. (**a**) Schematic of the silicon photonic crystal nanobeam laser structure suspended in air with a monolayer MoTe2 on top [114]. Reproduced with permission from Nature Nanotechnology; published by Springer Nature, 2017. (**b**) L3-type photonic cavity laser with multilayer $MoTe_2$ gain material on top [115]. Reproduced with permission from Laser & Photonics Reviews; published by John Wiley and Sons, 2018. (**c**) The illustration of the energy band of $WSe_2/MoSe_2$ heterojunction [113]. Reproduced with permission from Small Science; published by John Wiley and Sons, 2021. (**d**) The image of the MoS_2/WSe_2 heterobilayer–Si photonic crystal integrated nanolaser [116]. Reproduced with permission from Science Advances; published by the American Association for the Advancement of Science, 2019.

4.2. Microdisk Cavity-Based Nanolasers

Microdisks possessing low loss and high-quality whispering gallery modes (WGMs) have gained interest in the field of high-performance lasers due to their ability to efficiently confine light, which contributes to the potential for achieving ultralow-threshold lasing [109]. Ye et al. reported a WGM cavity-based laser with lasing emission at cryogenic temperature by embedding WS_2 between Si_3N_4 and hydrogen silsesquioxane (HSQ) microdisks [109]. The excitonic lasing peak can be achieved at 612 nm and the Q factor is 2604. This sandwiched structure (Figure 9a) provides both enhanced optical mode overlaps and good material protection. Salehzadeh et al. successfully demonstrated room-temperature lasing from 2D TMDC gain material by embedding bilayer MoS_2 at the interface between a free-standing SiO_2 microdisk and microsphere, leading to a high Q factor of 2600–3300 [117]. The structure is shown in Figure 9b. This nanolaser exhibited multiple photoluminescence (PL) peaks within the wavelength range of 600 to 800 nm. Notably, the threshold for lasing was measured to be around 5 μW under CW operation at room temperature. The exceptional performance exhibited by the lasing device can be attributed to two primary factors. Firstly, the large gain offered by the 2D TMDCs. Secondly, the strong coupling between the 2D MoS_2 gain material and the optical modes within the distinctive optical cavity promotes effective light–matter interactions. As shown in Figure 9c, a thin SiO_2 microdisk cavity with a notch defect is integrated with a chemically enhanced bilayer MoS_2 flake [118]. This work is reported by Reed et al. The notch is designed to facilitate optical excitation and aid in the extraction of cavity emission. This design results in a Q factor around 1000 and a significant enhancement of 20-fold in the PL intensity compared to that observed from as-exfoliated monolayers on the microdisk. This lasing device has a tunable lasing wavelength of 650–700 nm. To achieve enhanced emission, Duong et al. employed the coupling of WSe_2 monolayers with circular Bragg grating (CBG) structures [119]. Figure 9d illustrates the structure of the CBG, which consists of a central nanoscale disk surrounded by periodic ring antennas. The symmetric structure improves the directionality of emitted laser light at 756 nm. A notable enhancement in PL is observed, with approximately a 3-times increase at room temperature and a 7-times increase at 77 K. Typically, the integration is achieved using the transfer method, which is not suitable for large-scale production and often leads to a significant decrease in the quality factor of the microcavity during the transfer process [19]. Recently, Liu et al. presented a transfer-free excitonic nanolaser array operating at room temperature (Figure 9e) [120]. This was achieved by embedding a continuous monolayer of WS_2 between Si_3N_4 microdisks and Al_2O_3. Compared to the transfer method, the optical confinement factor in this study was found to be 4.8-times higher. This $Si_3N_4/WS_2/Al_2O$ nanolaser has multiple emission peaks ranging from 640 nm to 662 nm with a high Q factor of 3766.

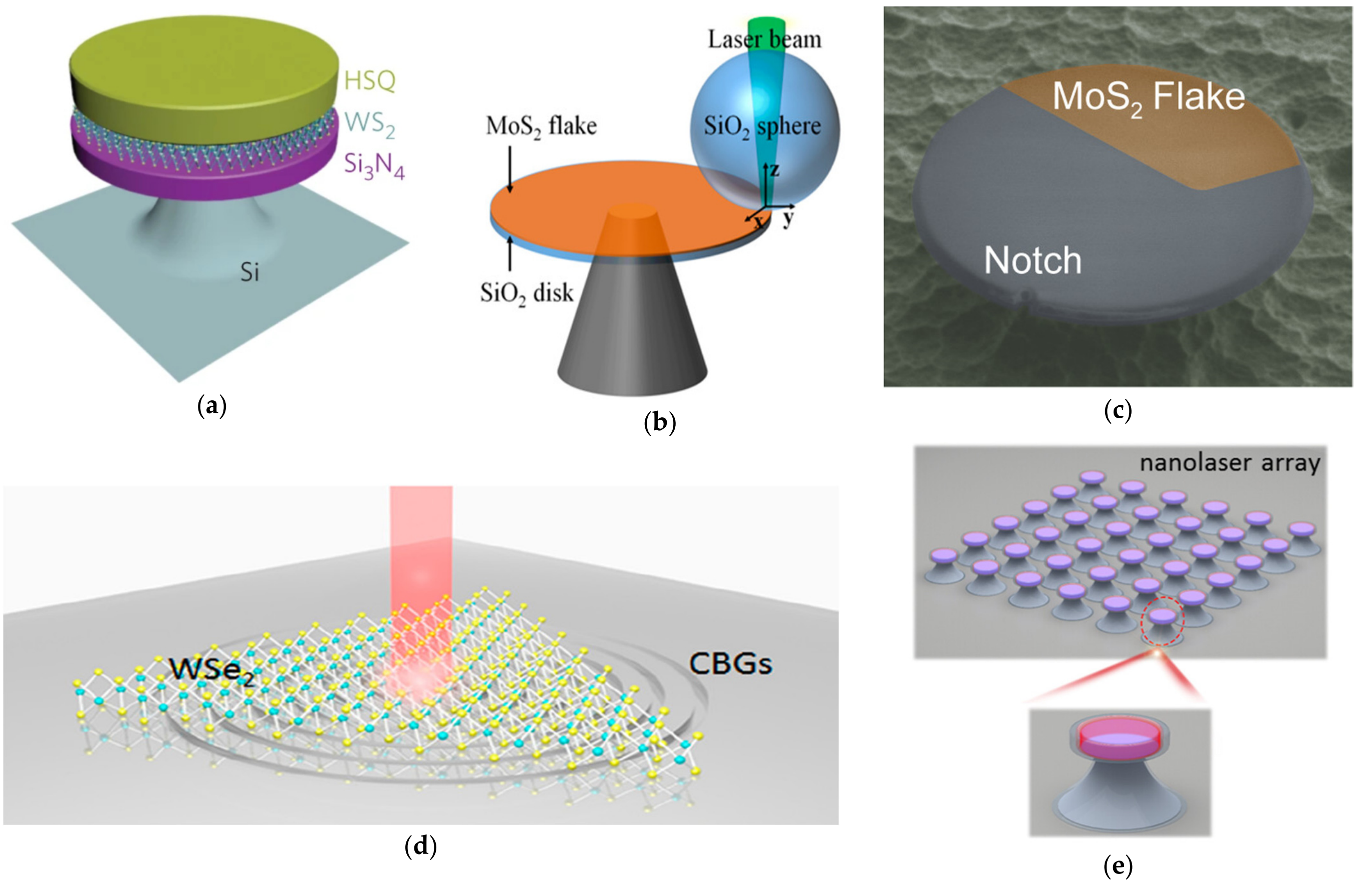

Figure 9. (**a**) Schematic image of a monolayer WS_2 microdisk laser with a $Si_3N_4/WS_2/Al_2O_3$ sandwich structure [109]. Reproduced with permission from Nature Photonics; published by Springer Nature, 2015. (**b**) Schematic configuration of the coupled microsphere/microdisk optical cavity with the incorporation of 2D MoS_2 [117]. Reproduced with permission from Nano Letters; published by the American Chemical Society, 2015. (**c**) SEM image of a MoS_2-coupled microdisk cavity laser [118]. Reproduced with permission from Nano Letters; published by the American Chemical Society, 2015. (**d**) Schematic of a WSe_2 monolayer laser on top of a circular Bragg grating (CBG) structure [119]. Reproduced with permission from ACS Photonics; published by the American Chemical Society, 2018. (**e**) Schematic of the monolayer WS_2 RT excitonic nanolaser array and the schematic images of a single nanolaser [120]. Reproduced with permission from ACS Photonics; published by the American Chemical Society, 2023.

5. Colloidal Quantum-Dot Lasers

Colloidal quantum dots (CQDs) as solution-processable semiconducting materials have drawn lots of interest for their potential for next-generation optoelectronic devices including lasers. QDs have a size-tunable bandgap, E_g. In QDs, the movement of carriers is limited in all three dimensions, reflecting a state of zero-dimension (0D) confinement. Due to the spatial restrictions placed on electronic wavefunctions, QDs demonstrate distinct electronic states (Figure 10) [121]. The energy of these states is dependent on the dimensions of the particle. The change in the bandgap due to quantum confinement, denoted as

$\Delta E_{conf} = E_g - E_{g,bulk}$, is proportional to $1/R^2$, where r is the radius of spherical QDs, and $E_{g,bulk}$ is the bandgap of the material in its bulk form [122]. This shift in the bandgap E_g is particularly significant for such nanocrystals because QDs can have an average radius ranging from 1 to 10 nm [123]. This tunable bandgap can achieve emission ranges from UV to infrared wavelength, which is greatly advantageous for applications in light-emission technologies, particularly in lasing. It can assist in filling gaps that are inaccessible with conventional semiconductor lasers. In addition, the discrete energy states of QDs are advantageous for lasing applications because of the broad separation between electronic states, which prevents thermal depopulation of the band-edge electron and hole levels (Figure 10) [124]. This consequently reduces the lasing threshold.

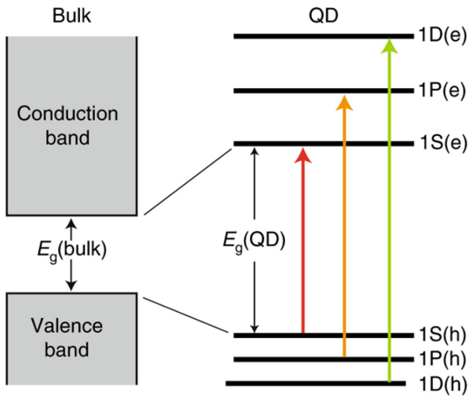

Figure 10. Band diagram of bulk semiconductor materials (left) and QD band diagram with discrete states due to 0D confinement. The red, orange, and green arrows represent the discrete light absorption [121]. Reproduced with permission from Nature Photonics; published by Springer Nature, 2021.

CQD lasers are currently still at the lab stage. The main challenge that persists is the short lifetime of the CQD gain medium, primarily due to intrinsic non-radiative Auger recombination [125]. This issue particularly hinders the achievement of lasing with continuous-wave optical and direct-current electrical excitation [126]. Furthermore, the nonradiative Auger recombination surpasses the amplification of light by swiftly annihilating the exciton population, resulting in high gain thresholds [127]. In the past few years, significant effort has been devoted to overcoming this main challenge and successfully achieving lasing.

As Adachi et al. reported, the primary factor contributing to the nanosecond operation of CQD lasing is the combination of swift heat injection from the pump source, inadequate heat dissipation, and a threshold that is strongly influenced by temperature [128]. This group successfully demonstrated the ability for microsecond lasing by utilizing ultra-compact CdSe-CdS-ZnS core–shell–shell CQD films on a thermally conductive substrate, as shown in Figure 11a [128]. This structure effectively reduced heat buildup. The lasing process demonstrated a high modal gain of 1200 cm^{-1} and an extremely low threshold for amplified spontaneous emission, with an average peak power of approximately 50 kW/cm^{-2}. This achievement relies on an optical structure that efficiently dissipates heat while minimizing modal loss. These findings indicate the potential to achieve continuous-wave (CW) lasing utilizing CQD nanomaterials. Fan et al. successfully achieved the CW operation of CQD-based lasers by utilizing CQDs with suppressed Auger recombination [126]. They integrated a film of biaxially strained CdSe-CdS core–shell CQDs within a photonic crystal distributed feedback (PC-DFB) optical cavity, as shown in Figure 11b [126]. To improve thermal conductivity in the QD layer, they incorporated short-chain ligands. And for efficient heat dissipation, they utilized thermally conductive MgF_2 substrates. Under CW excitation, they demonstrated lasing with a threshold of 8.4 kW/cm^{-2}. The sample exhibited reliable operation for a duration of 30 min. Kozlov et al. reported a charged-exciton approach to hinder Anger decay, which makes it possible to realize the lasing threshold to values below the single-exciton-per-dot limit [129]. In the experiment, a device consisting of CdSe/$Cd_xZn_{1-x}Se$/$ZnSe_{0.5}S_{0.5}$/ZnS continuously graded CQDs (cg-CQDs) assembled on a second-order DFB resonator (Figure 11c) is placed in tetrahydrofuran. To introduce additional electrons to the CQDs through photochemical charging, controlled amounts of a photoreductant ($LiEt_3BH$) are added to the tetrahydrofuran. The notable advantage of this approach is that it led to a four-times reduction in the lasing threshold compared to using neutral CQDs. This demonstrates that utilizing the charged-exciton gain approach allows for achieving extremely low lasing thresholds below the single-exciton-per-dot limit, and also extends the duration of the gain lifetime. Roh et al. have successfully created an LED-like multilayered DFB laser by employing cg-CQDs with suppressed Auger recombination as the gain medium. A p-i-n structure consists of a TCTA hole transport layer, a CQD active layer, and a ZnO electron transport layer. The laser incorporates a second-order DFB grating, which is integrated into a low refractive index ITO electrode, serving as an optical cavity [130], This laser (Figure 11d) can achieve signal-mode lasing at 629 nm, and a very low lasing threshold of 18.8 μJ cm^{-2} even with an ultra-thin gain medium containing only three CQD monolayers (50 nm). It is worth noting that this device can also operate as an electrically pumped LED.

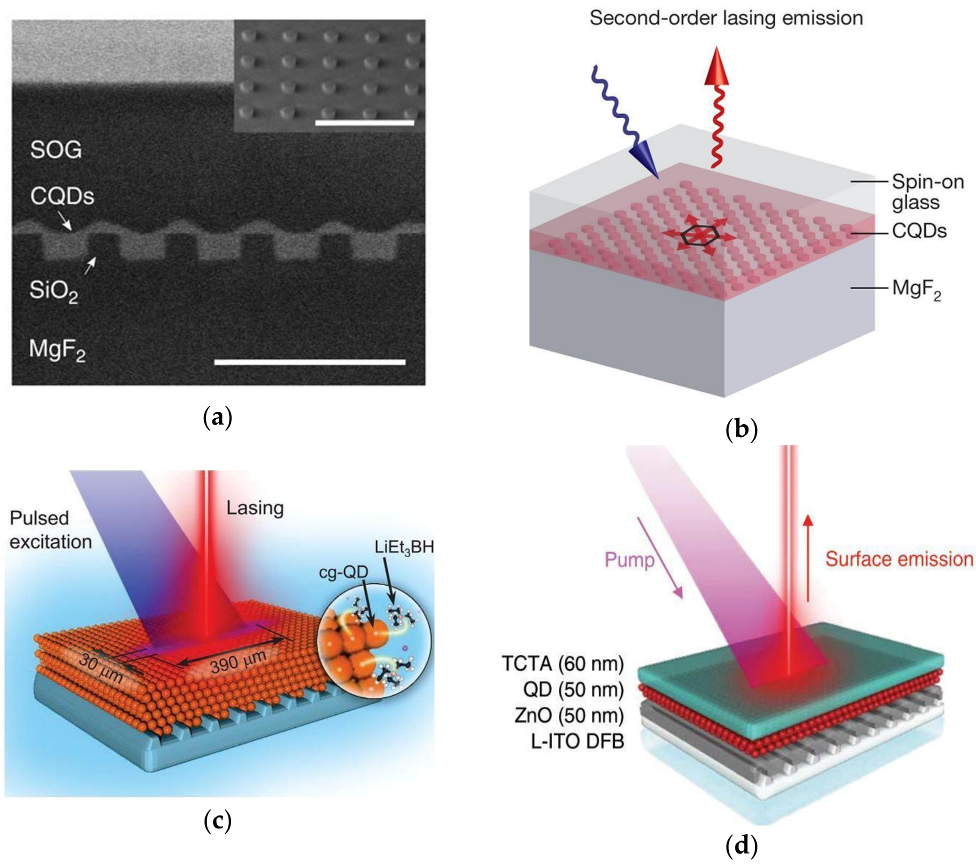

Figure 11. (**a**) Cross-section SEM image of a 2D distributed feedback (DFB) array structure on a thermally conductive MgF_2 substrate [128]. Reproduced with permission from Nature Communications; published by Springer Nature, 2015. (**b**) Schematic of a CdSe-CdS core–shell CQD laser integrated with a PC-DFB optical cavity [126]. Reproduced with permission from Nature; published by Springer Nature, 2017. (**c**) Schematics of a cg-QDDFB laser. This device is immersed into a $LiEt_3BH$ solution in THF [129]. Reproduced with permission from Science; published by the American Association for the Advancement of Science, 2019. (**d**) Schematic illustration of an optically pumped multilayered DFB laser in a traditional p-i-n QD-LED structure [130]. Reproduced with permission from Nature Communications; published by Springer Nature, 2020.

Pb-chalcogenide CQDs are highly attractive materials for their potential applications as tunable laser media covering a wide range of the infrared spectrum. In a study by Taghipour et al., a binary blend of PbS CQDs and ZnO nanocrystals was utilized to passivate the in-gap trap states of the PbS CQD gain medium [127]. This approach effectively suppressed trap-assisted Auger recombination, as demonstrated by a fivefold increase in the Auger lifetime. The integration of this binary blend into a DFB resonator (Figure 12) resulted in single-mode lasing emission at 1650 nm, with a narrow linewidth of 1.23 nm and a low threshold of approximately 385 μJ cm^{-2}. Remarkably, continuous operation of this PbS CQD laser was achieved for 5 h at room temperature. Recently, Taghipour et al. reported PbS/PbSSe core/alloyed-shell CQDs as an infrared gain medium that results in a highly suppressed Auger recombination with a lifetime of 485 ps [131]. By doping the engineered core/shell CQDs to nearly fill the first excited state, a remarkable reduction in the lasing threshold to 160 μJ cm^{-2} is demonstrated. The doped CQD/DFB laser operates at 1670 nm with a linewidth of approximately 1 nm.

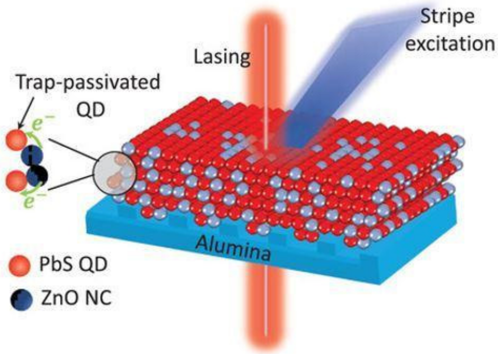

Figure 12. Schematic representation of the DFB laser under optical pumping. Red and blue dots symbolize PbS-emitter QDs and ZnO NCs, respectively [127]. Reproduced with permission from Advanced Materials; published by John Wiley and Sons, 2021.

As previously discussed, alongside advancements in the excitation scheme of CQD lasers, scientists have merged CQDs with high-quality cavities, enabling the emission of light that is spatially and temporally coherent in a well-defined manner. The Si photonics platform has garnered significant attention due to its capacity to fabricate high-precision photonic cavities and its compatibility with cost-effective complementary metal-oxide-semiconductor (CMOS) fabrication processes. Chang et al. reported a room-temperature lasing operation of a novel CQD-PC band-edge laser [132]. Core–shell–shell-type CdSe/CdS/ZnS CQDs were spin-coated as the gain material onto a passive Si_3N_4 2D square lattice PC backbone slab (Figure 13a). Upon reaching the lasing threshold of 300 μJ cm^{-2}, the CQD-PC laser exhibited an emission peak of approximately 615 nm. Xie et al. presented the first demonstration of an on-chip microdisk laser that integrates CQDs with planar SiN waveguides on a Si substrate [133]. The microdisk structure comprises a sandwich of SiN/CQD/SiN (Figure 13b), which enables a high Q of 1000. The design maximizes the optical confinement within the central CQD layer and achieves a lasing peak at 630 nm. This CQD laser with only a 7 μm diameter disk demonstrates an exceptionally low threshold of 27 μJ cm^{-2} at room temperature. On-chip solution-processable wavelength-tunable CQD lasers have a bright future, as they offer significant advantages for highly compact photonic integrated circuits working in the most important 1300 and 1550 nm communication bands.

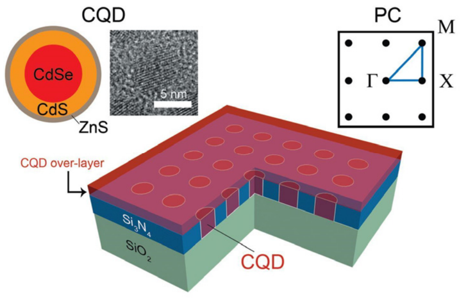

(**a**)

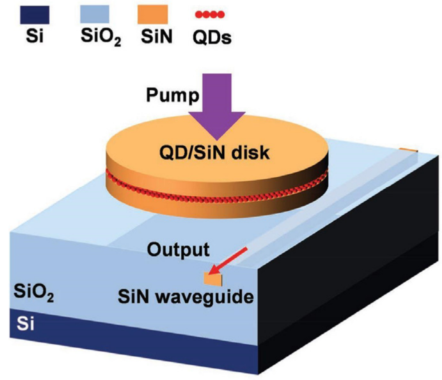

(**b**)

Figure 13. (**a**) Schematic of the CdSe/CdS/ZnS core–shell–shell CQD-PC band-edge laser with a Si_3N_4 waveguide on a SiO_2-cladding/Si substrate [132]. Reproduced with permission from Nanoscale; published by the Royal Society of Chemistry, 2009. (**b**) Configuration of a CQD/SiN disk with a SiN waveguide. A layer of CQDs is embedded in the SiN disk [133]. Reproduced with permission from Advanced Materials; published by John Wiley and Sons, 2017.

Up to now, lasing based on CQD gain materials has been exclusively triggered by optical pumping. The next step will be to achieve electrical pumping CQD lasers, which is more practically desirable due to its ease of integration and control. To date, optical gain in such nanocrystals has been achieved through direct-current electrical pumping [134], and there have also been successful demonstrations of amplified spontaneous emission from electrically pumped CQDs [135]. We believe that through continued advancements in materials science and device technology, solution-processed lasers utilizing CQDs will become key players in diverse photonic and optoelectronic applications. They have the potential to become a compelling complement to epitaxial semiconductor lasers in the near future.

6. Conclusions and Perspectives

On-chip lasers have made great strides over the past decade. Here, we have presented the most common approaches toward achieving integrated lasers on silicon. The epitaxial growth of Ge and GeSn on Si as a platform for on-chip lasers has shown promising results. By inducing a tensile strain in the material to alter its bandgap, lasing has been demonstrated. However, the inherent indirect bandgap of Group IV materials presents a challenge for achieving efficient, scalable integrated lasers. We have also explored photonic crystal cavity-based nanolasers and microdisk cavity-based nanolasers, both of which are 2D-material-based lasers. The ease of integration with Si and the demonstration of quantum confinement makes 2D materials an appealing platform to realize integrated lasers. However, their low quantum yield is a significant drawback.

The most widely explored platform for integrating lasers on Si is III–V materials. The direct bandgap of III–V materials and the plethora of integration techniques gives III–V-material lasers a lot of potential. We reviewed the recent progress made in heterogeneous and monolithically integrated lasers. Monolithically grown III–V quantum-dot lasers with a long lifetime, high output power, and low-threshold current densities have been realized, far superior to their quantum-well counterparts. Although results are promising, more research is required to achieve the reliable, power-efficient, high-density integration of III–V lasers on Si chips. Lastly, we explored the potential of CQDs to realize on-chip lasers. As their bandgap is tunable, they can achieve emission ranges from UV to infrared. CQD lasers are still in their infancy, with major hurdles such as an electrically pumped scheme. However, lasing has been demonstrated in various CQDs and hence shows a promising future for integrating them into silicon chips.

The potential of silicon photonics, or silicon-based photonic integrated circuits (PICs), is highly compelling due to their seamless integration capability with the well-established CMOS fabrication technology in the microelectronics industry, which enables the achievement of high-volume yields at low die costs, excellent uniformity, and significant scalability. The achievement of on-chip light sources represents a significant milestone in advancing the complete integration of silicon-based PICs. This advancement will be critical for several potential applications including optical communications and interconnects, LIDAR, chemical and biological sensing, and optical computing.

Future research is imperative to enhance laser quality, increase yield, and develop cost-effective integration methods. Commercial III–V-material on-chip lasers primarily rely on heterogeneous integration techniques. Although monumental progress has been made in these techniques over the past few years, issues such as high cost, low yield, and limited scalability persist. Various strategies, such as 3D integration techniques and using SiN, are being pursued to address some of these limitations. Monolithic integration is an attractive alternative due to its low cost and high integration density. However, it introduces a high density of crystalline defects, significantly degrading the laser's performance. Exploring methods of reducing these defects is paramount to advance monolithic integration toward high-density, large-scale silicon photonic integration. In the field of 2D materials for on-chip lasers, achieving large-scale synthesis of high-quality uniform 2DMs with superior optical, electrical, and mechanical properties is an important step forward. A lower threshold and higher output power could be achieved by optimizing the structure of the device in the future. The majority of currently reported 2D-material-based lasers rely on optical pumping. Hence, a notable challenge lies in realizing electrically pumped on-chip lasers utilizing 2DMs, and it should be tackled in the following years. The development of on-chip lasers utilizing CQDs is still in its early stages. As the field advances toward integrated photonics, there is a compelling need to realize electrically pumped CQD lasers. We anticipate that through ongoing progress in materials science and device optimization, solution-processed CQD lasers will emerge as an important player in Si-integrated lasers.

Author Contributions: Conceptualization, J.Z., A.G.S. and X.W.; formal analysis, J.Z. and A.G.S.; investigation, J.Z. and A.G.S.; resources, J.Z. and A.G.S.; writing—original draft preparation, J.Z. and A.G.S.; writing—review and editing, X.W.; supervision, X.W.; project administration, X.W.; funding acquisition, X.W. All authors have read and agreed to the published version of the manuscript.

Funding: This research was funded by the Natural Sciences and Engineering Research Council of Canada (NSERC) Discovery Grants program, grant number RGPIN-2019-04664.

Data Availability Statement: No new data were created or analyzed in this study. Data sharing is not applicable to this article.

Acknowledgments: Aadithya G. Shankar acknowledges the support from the Mitacs Globalink Research Internship.

Conflicts of Interest: The authors declare no conflicts of interest.

References

1. Nagarajan, R.; Joyner, C.H.; Schneider, R.P.; Bostak, J.S.; Butrie, T.; Dentai, A.G.; Dominic, V.G.; Evans, P.W.; Kato, M.; Kauffman, M.; et al. Large-scale photonic integrated circuits. *IEEE J. Sel. Top. Quantum Electron.* **2005**, *11*, 50–65. [CrossRef]
2. Arafin, S.; Coldren, L.A. Advanced InP photonic integrated circuits for communication and sensing. *IEEE J. Sel. Top. Quantum Electron.* **2017**, *24*, 1–12. [CrossRef]
3. Zhou, Z.; Ou, X.; Fang, Y.; Alkhazraji, E.; Xu, R.; Wan, Y.; Bowers, J.E. Prospects and applications of on-chip lasers. *Elight* **2023**, *3*, 1–25. [CrossRef] [PubMed]
4. Li, N.; Chen, G.; Ng, D.K.T.; Lim, L.W.; Xue, J.; Ho, C.P.; Fu, Y.H.; Lee, L.Y.T. Integrated lasers on silicon at communication wavelength: A progress review. *Adv. Opt. Mater.* **2022**, *10*, 2201008. [CrossRef]
5. Xiang, C.; Bowers, S.M.; Bjorlin, A.; Blum, R.; Bowers, J.E. Perspective on the future of silicon photonics and electronics. *Appl. Phys. Lett.* **2021**, *118*, 220501. [CrossRef]
6. Lockwood, D.J.; Pavesi, L. *Silicon Photonics IV*; Springer: Berlin/Heidelberg, Germany, 2021; Volume 139. [CrossRef]

7. Dai, D.; Bauters, J.; Bowers, J.E. Passive technologies for future large-scale photonic integrated circuits on silicon: Polarization handling, light non-reciprocity and loss reduction. *Light Sci. Appl.* **2012**, *1*, e1. [CrossRef]
8. Heck, M.J.R.; Bauters, J.F.; Davenport, M.L.; Spencer, D.T.; Bowers, J.E. Ultra-low loss waveguide platform and its integration with silicon photonics. *Laser Photonics Rev.* **2014**, *8*, 667–686. [CrossRef]
9. Su, Y.; Zhang, Y.; Qiu, C.; Guo, X.; Sun, L. Silicon photonic platform for passive waveguide devices: Materials, fabrication, and applications. *Adv. Mater. Technol.* **2020**, *5*, 1901153. [CrossRef]
10. Reed, G.T.; Mashanovich, G.; Gardes, F.Y.; Thomson, D.J. Silicon optical modulators. *Nat. Photonics* **2010**, *4*, 518–526. [CrossRef]
11. Witzens, J. High-speed silicon photonics modulators. *Proc. IEEE* **2018**, *106*, 2158–2182. [CrossRef]
12. Rahim, A.; Hermans, A.; Wohlfeil, B.; Petousi, D.; Kuyken, B.; Van Thourhout, D.; Baets, R. Taking silicon photonics modulators to a higher performance level: State-of-the-art and a review of new technologies. *Adv. Photonics* **2021**, *3*, 024003. [CrossRef]
13. Piels, M.; Bowers, J.E. Photodetectors for silicon photonic integrated circuits. In *Photodetectors*; Elsevier: Amsterdam, The Netherlands, 2023; pp. 419–436. [CrossRef]
14. Liu, C.; Guo, J.; Yu, L.; Li, J.; Zhang, M.; Li, H.; Shi, Y.; Dai, D. Silicon/2D-material photodetectors: From near-infrared to mid-infrared. *Light Sci. Appl.* **2021**, *10*, 123. [CrossRef] [PubMed]
15. Mauthe, S.; Baumgartner, Y.; Sousa, M.; Ding, Q.; Rossell, M.D.; Schenk, A.; Czornomaz, L.; Moselund, K.E. High-speed III–V nanowire photodetector monolithically integrated on Si. *Nat. Commun.* **2020**, *11*, 4565. [CrossRef] [PubMed]
16. Wen, P.; Tiwari, P.; Mauthe, S.; Schmid, H.; Sousa, M.; Scherrer, M.; Baumann, M.; Bitachon, B.I.; Leuthold, J.; Gotsmann, B.; et al. Waveguide coupled III-V photodiodes monolithically integrated on Si. *Nat. Commun.* **2022**, *13*, 909. [CrossRef]
17. Xu, Q.; Hu, J.; Wang, X. On-chip Ge, InGaAs, and colloidal quantum dot photodetectors: Comparisons for application in silicon photonics. *J. Opt. Soc. Am. B* **2021**, *38*, 194–200. [CrossRef]
18. Zhou, Z.; Yin, B.; Michel, J. On-chip light sources for silicon photonics. *Light Sci. Appl.* **2015**, *4*, e358. [CrossRef]
19. Shi, Y.; Zhang, Y.; Wan, Y.; Yu, Y.; Zhang, Y.; Hu, X.; Pan, B. Silicon photonics for high-capacity data communications. *Photonics Res.* **2022**, *10*, A106–A134. [CrossRef]
20. Liu, J.; Kimerling, L.C.; Michel, J. Monolithic Ge-on-Si Lasers for Large-Scale Electronic-Photonic Integration. *Semicond. Sci. Technol.* **2012**, *27*, 094006. [CrossRef]
21. Moutanabbir, O.; Assali, S.; Gong, X.; O'Reilly, E.; Broderick, C.A.; Marzban, B.; Witzens, J.; Du, W.; Yu, S.-Q.; Chelnokov, A.; et al. Monolithic Infrared Silicon Photonics: The Rise of (Si) GeSn Semiconductors. *Appl. Phys. Lett.* **2021**, *118*, 110501. [CrossRef]
22. Ye, H.; Yu, J. Germanium Epitaxy on Silicon. *Sci. Technol. Adv. Mater.* **2014**, *15*, 024601. [CrossRef]
23. Liu, J.; Sun, X.; Pan, D.; Wang, X.; Kimerling, L.C.; Koch, T.L.; Michel, J. Tensile-Strained, n-Type Ge as a Gain Medium for Monolithic Laser Integration on Si. *Opt. Express* **2007**, *15*, 11272–11277. [CrossRef]
24. Liu, J.; Sun, X.; Camacho-Aguilera, R.; Kimerling, L.C.; Michel, J. Ge-on-Si Laser Operating at Room Temperature. *Opt. Lett.* **2010**, *35*, 679–681. [CrossRef]
25. Liang, D.; Bowers, J.E. Recent Progress in Lasers on Silicon. *Nat. Photonics* **2010**, *4*, 511–517. [CrossRef]
26. Reboud, V.; Buca, D.; Sigg, H.; Hartmann, J.M.; Ikonic, Z.; Pauc, N.; Calvo, V.; Rodriguez, P.; Chelnokov, A. Lasing in Group-IV Materials. In *Silicon Photonics IV*; Springer: Berlin/Heidelberg, Germany, 2021; pp. 105–195.
27. Stange, D.; von den Driesch, N.; Zabel, T.; Armand-Pilon, F.; Rainko, D.; Marzban, B.; Zaumseil, P.; Hartmann, J.-M.; Ikonic, Z.; Capellini, G.; et al. GeSn/SiGeSn Heterostructure and Multi Quantum Well Lasers. *ACS Photonics* **2018**, *5*, 4628–4636. [CrossRef]
28. Bao, S.; Kim, D.; Onwukaeme, C.; Gupta, S.; Saraswat, K.; Lee, K.H.; Kim, Y.; Min, Y.; Jung, Y.; Nam, D.; et al. Low-threshold optically pumped lasing in highly strained germanium nanowires. *Nat. Commun.* **2017**, *8*, 1845. [CrossRef]
29. Zhou, Y.; Dou, W.; Du, W.; Ojo, S.; Tran, H.; Ghetmiri, S.A.; Liu, J.; Sun, G.; Soref, R.; Margetis, J.; et al. Optically Pumped GeSn Lasers Operating at 270 K with Broad Waveguide Structures on Si. *ACS Photonics* **2019**, *6*, 1434–1441. [CrossRef]
30. Chrétien, J.; Pauc, N.; Armand Pilon, F.; Bertrand, M.; Thai, Q.-M.; Casiez, L.; Bernier, N.; Dansas, H.; Gergaud, P.; Delamadeleine, E.; et al. GeSn Lasers Covering a Wide Wavelength Range Thanks to Uniaxial Tensile Strain. *ACS Photonics* **2019**, *6*, 2462–2469. [CrossRef]
31. Elbaz, A.; Buca, D.; von den Driesch, N.; Pantzas, K.; Patriarche, G.; Zerounian, N.; Herth, E.; Checoury, X.; Sauvage, S.; Sagnes, I.; et al. Ultra-low-threshold continuous-wave and pulsed lasing in tensile-strained GeSn alloys. *Nat. Photonics* **2020**, *14*, 375–382. [CrossRef]
32. Wirths, S.; Geiger, R.; Von Den Driesch, N.; Mussler, G.; Stoica, T.; Mantl, S.; Ikonic, Z.; Luysberg, M.; Chiussi, S.; Hartmann, J.-M.; et al. Lasing in Direct-Bandgap GeSn Alloy Grown on Si. *Nat. Photonics* **2015**, *9*, 88–92. [CrossRef]
33. Liu, J. Monolithically Integrated Ge-on-Si Active Photonics. *Photonics* **2014**, *1*, 162–197. [CrossRef]
34. Zhou, Y.; Miao, Y.; Ojo, S.; Tran, H.; Abernathy, G.; Grant, J.M.; Amoah, S.; Salamo, G.; Du, W.; Liu, J.; et al. Electri-cally injected GeSn lasers on Si operating up to 100 K. *Optica* **2020**, *7*, 924–928. [CrossRef]
35. Xiang, C.; Jin, W.; Huang, D.; Tran, M.A.; Guo, J.; Wan, Y.; Xie, W.; Kurczveil, G.; Netherton, A.; Bowers, J.E.; et al. High-performance silicon photonics using heterogeneous integration. *IEEE J. Sel. Top. Quantum Electron.* **2021**, *28*, 1–15. [CrossRef]
36. Liang, D.; Bowers, J.E. Recent progress in heterogeneous III-V-on-silicon photonic integration. *Light: Adv. Manuf.* **2021**, *2*, 59–83. [CrossRef]
37. Wan, Y.; Norman, J.; Liu, S.; Liu, A.; Bowers, J.E. Quantum dot lasers and amplifiers on silicon: Recent advances and future developments. *IEEE Nanotechnol. Mag.* **2021**, *15*, 8–22. [CrossRef]

38. Shang, C.; Wan, Y.; Selvidge, J.; Hughes, E.; Herrick, R.; Mukherjee, K.; Duan, J.; Grillot, F.; Chow, W.; Bowers, J.E.; et al. Perspectives on advances in quantum dot lasers and integration with Si photonic integrated circuits. *ACS Photonics* **2021**, *8*, 2555–2566. [CrossRef]
39. He, S.; Li, M. Multi-scale texturing for a-Si/mc-Si thin-film tandem solar cells. *AIP Adv.* **2018**, *8*, 3. [CrossRef]
40. Hu, Y.; Liang, D.; Mukherjee, K.; Li, Y.; Zhang, C.; Kurczveil, G.; Huang, X.; Beausoleil, R.G. III/V-on-Si MQW lasers by using a novel photonic integration method of regrowth on a bonding template. *Light Sci. Appl.* **2019**, *8*, 93. [CrossRef]
41. Bian, Y.; Ramachandran, K.; Peng, B.; Hedrick, B.; Mills, S.; Donegan, K.; Esopi, M.; Hirokawa, T.; Jacob, A.; Karra, V.; et al. Integrated laser attach technology on a monolithic silicon photonics platform. In Proceedings of the 2021 IEEE 71st Electronic Components and Technology Conference (ECTC), San Diego, CA, USA, 1 June–4 July 2021; pp. 237–244. [CrossRef]
42. Moscoso-Mártir, A.; Merget, F.; Mueller, J.; Hauck, J.; Romero-García, S.; Shen, B.; Lelarge, F.; Brenot, R.; Garreau, A.; Men-tovich, E.; et al. Hybrid silicon photonics flip-chip laser integration with vertical self-alignment. In Proceedings of the Conference on Lasers and Electro-Optics/Pacific Rim; Optica Publishing Group, Singapore, 31 July–4 August 2017; p. s2069. [CrossRef]
43. Justice, J.; Bower, C.; Meitl, M.; Mooney, M.B.; Gubbins, M.A.; Corbett, B. Wafer-scale integration of group III–V lasers on silicon using transfer printing of epitaxial layers. *Nat. Photonics* **2012**, *6*, 610–614. [CrossRef]
44. Zhang, J.; Muliuk, G.; Juvert, J.; Kumari, S.; Goyvaerts, J.; Haq, B.; Op de Beeck, C.; Kuyken, B.; Morthier, G.; Van Thourhout, D.; et al. III-V-on-Si photonic integrated circuits realized using micro-transfer-printing. *APL Photonics* **2019**, *4*, 11. [CrossRef]
45. Roelkens, G.; Van Campenhout, J.; Brouckaert, J.; Van Thourhout, D.; Baets, R.; Romeo, P.R.; Regreny, P.; Kazmierczak, A.; Seassal, C.; Letartre, X.; et al. III-V/Si photonics by die-to-wafer bonding. *Mater. Today* **2007**, *10*, 36–43. [CrossRef]
46. Sparks, D.; Queen, G.; Weston, R.; Woodward, G.; Putty, M.; Jordan, L.; Zarabadi, S.; Jayakar, K. Wafer-to-wafer bonding of nonplanarized MEMS surfaces using solder. *J. Micromech. Microeng.* **2001**, *11*, 630. [CrossRef]
47. Maharbiz, M.M.; Cohn, M.B.; Howe, R.T.; Horowitz, R.; Pisano, A.P. Batch micropackaging by compression-bonded wafer-wafer transfer. In Proceedings of the Technical Digest. IEEE International MEMS 99 Conference. Twelfth IEEE International Conference on Micro Electro Mechanical Systems (Cat. No. 99CH36291), Orlando, FL, USA, 21 January 1999; IEEE: Piscataway, NJ, USA; pp. 482–489. [CrossRef]
48. Jongbaeg, K.; Mu, C.; Liwei, L. Ultrasonic bonding of In/Au and Al/Al for hermetic sealing of MEMS packaging. In Proceedings of the Technical Digest. MEMS 2002 IEEE International Conference. Fifteenth IEEE International Conference on Micro Electro Mechanical Systems (Cat. No.02CH37266), Las Vegas, NV, USA, 24 January 2002. [CrossRef]
49. Cheng, Y.T.; Lin, L.; Najafi, K. Localized silicon fusion and eutectic bonding for MEMS fabrication and packaging. *J. Microelectromech. Syst.* **2000**, *9*, 3–8. [CrossRef]
50. Audet, S.A.; Edenfeld, K.M. Integrated sensor wafer-level packaging. In Proceedings of the International Solid State Sensors and Actuators Conference (Transducers '97), Chicago, IL, USA, 19 June 1997; pp. 287–289. [CrossRef]
51. Luo, X.; Cao, Y.; Song, J.; Hu, X.; Cheng, Y.; Li, C.; Liu, C.; Liow, T.-Y.; Yu, M.; Wang, H.; et al. High-throughput multiple dies-to-wafer bonding technology and III/V-on-Si hybrid lasers for heterogeneous integration of optoelectronic integrated circuits. *Front. Mater.* **2015**, *2*, 28. [CrossRef]
52. Liang, D.; Huang, X.; Kurczveil, G.; Fiorentino, M.; Beausoleil, R.G. Integrated finely tunable microring laser on silicon. *Nat. Photonics* **2016**, *10*, 719–722. [CrossRef]
53. Fujii, T.; Sato, T.; Takeda, K.; Hasebe, K.; Kakitsuka, T.; Matsuo, S. Epitaxial growth of InP to bury directly bonded thin active layer on SiO2/Si substrate for fabricating distributed feedback lasers on silicon. *IET Optoelectron.* **2015**, *9*, 151–157. [CrossRef]
54. Wang, J.; Ren, X.; Deng, C.; Hu, H.; He, Y.; Cheng, Z.; Ma, H.; Wang, Q.; Huang, Y.; Yan, X. Extremely low-threshold current density InGaAs/AlGaAs quantum-well lasers on silicon. *J. Light. Technol.* **2015**, *33*, 3163–3169. [CrossRef]
55. Wang, R.; Sprengel, S.; Boehm, G.; Muneeb, M.; Baets, R.; Amann, M.C.; Roelkens, G. 2.3 μm range InP-based type-II quantum well Fabry-Perot lasers heterogeneously integrated on a silicon photonic integrated circuit. *Opt. Express* **2016**, *24*, 21081–21089. [CrossRef]
56. Shi, B.; Zhao, H.; Wang, L.; Song, B.; Brunelli, S.T.S.; Klamkin, J. Continuous-wave electrically pumped 1550 nm lasers epitaxially grown on on-axis (001) silicon. *Optica* **2019**, *6*, 1507–1514. [CrossRef]
57. Chow, W.W.; Wan, Y.; Bowers, J.E.; Grillot, F. Analysis of the spontaneous emission limited linewidth of an integrated III–V/SiN laser. *Laser Photonics Rev.* **2022**, *16*, 2100620. [CrossRef]
58. Alkhazraji, E.; Chow, W.W.; Grillot, F.; Bowers, J.E.; Wan, Y. Linewidth narrowing in self-injection-locked on-chip lasers. *Light Sci. Appl.* **2023**, *12*, 162. [CrossRef]
59. Uvin, S.; Kumari, S.; De Groote, A.; Verstuyft, S.; Lepage, G.; Verheyen, P.; Van Campenhout, J.; Morthier, G.; Van Thourhout, D.; Roelkens, G. 1.3 um InAs/GaAs quantum dot DFB laser integrated on a Si waveguide circuit by means of adhesive die-to-wafer bonding. *Opt. Express* **2018**, *26*, 18302–18309. [CrossRef] [PubMed]
60. Wan, Y.; Xiang, C.; Guo, J.; Koscica, R.; Kennedy, M.J.; Selvidge, J.; Zhang, Z.; Chang, L.; Xie, W.; Bowers, J.E. High speed evanescent quantum-dot lasers on Si. *Laser Photonics Rev.* **2021**, *15*, 2100057. [CrossRef]
61. Koscica, R.; Wan, Y.; He, W.; Kennedy, M.J.; Bowers, J.E. Heterogeneous integration of a III–V quantum dot laser on high thermal conductivity silicon carbide. *Opt. Lett.* **2023**, *48*, 2539–2542. [CrossRef]
62. Xiang, C.; Jin, W.; Guo, J.; Peters, J.D.; Kennedy, M.J.; Selvidge, J.; Morton, P.A.; Bowers, J.E. Narrow-linewidth III-V/Si/Si_3N_4 laser using multilayer heterogeneous integration. *Optica* **2020**, *7*, 20–21. [CrossRef]

63. Shen, B.; Chang, L.; Liu, J.; Wang, H.; Yang, Q.F.; Xiang, C.; Bowers, J.E. Integrated turnkey soliton microcombs. *Nature* **2020**, *582*, 365–369. [CrossRef]
64. Rizzo, A.; Novick, A.; Gopal, V.; Kim, B.Y.; Ji, X.; Daudlin, S.; Okawachi, Y.; Cheng, Q.; Lipson, M.; Bergman, K. Massively scalable Kerr comb-driven silicon photonic link. *Nat. Photonics* **2023**, *17*, 781–790. [CrossRef]
65. Xiang, C.; Liu, J.; Guo, J.; Chang, L.; Wang, R.N.; Weng, W.; Peters, J.; Xie, W.; Zhang, Z.; Bowers, J.E. Laser soliton microcombs heterogeneously integrated on silicon. *Science* **2021**, *373*, 99–103. [CrossRef] [PubMed]
66. Xiang, C.; Guo, J.; Jin, W.; Wu, L.; Peters, J.; Xie, W.; Bowers, J.E. High-performance lasers for fully integrated silicon nitride photonics. *Nat. Commun.* **2021**, *12*, 6650. [CrossRef] [PubMed]
67. Xiang, C.; Jin, W.; Terra, O.; Dong, B.; Wang, H.; Wu, L.; Guo, J.; Morin, T.J.; Hughes, E.; Peters, J.; et al. 3D integration enables ultralow-noise isolator-free lasers in silicon photonics. *Nature* **2023**, *620*, 78–85. [CrossRef] [PubMed]
68. Roelkens, G.; Liu, L.; Liang, D.; Jones, R.; Fang, A.; Koch, B.; Bowers, J. III-V/silicon photonics for on-chip and intra-chip optical interconnects. *Laser Photonics Rev.* **2010**, *4*, 751–779. [CrossRef]
69. Tang, M.; Park, J.-S.; Wang, Z.; Chen, S.; Jurczak, P.; Seeds, A.; Liu, H. Integration of III-V lasers on Si for Si photonics. *Prog. Quantum Electron.* **2019**, *66*, 1–18. [CrossRef]
70. Wang, Z.; Van Gasse, K.; Moskalenko, V.; Latkowski, S.; Bente, E.; Kuyken, B.; Roelkens, G. A III-V-on-Si ultra-dense comb laser. *Light: Sci. Appl.* **2017**, *6*, e16260. [CrossRef] [PubMed]
71. Norman, J.C.; Jung, D.; Wan, Y.; Bowers, J.E. Perspective: The future of quantum dot photonic integrated circuits. *APL Photonics* **2018**, *3*, 031301. [CrossRef]
72. Wang, Z.; Tian, B.; Pantouvaki, M.; Guo, W.; Absil, P.; Van Campenhout, J.; Merckling, C.; Van Thourhout, D. Room-temperature InP distributed feedback laser array directly grown on silicon. *Nat. Photonics* **2015**, *9*, 837–842. [CrossRef]
73. Windhorn, T.H.; Metze, G.M.; Tsaur, B.-Y.; Fan, J.C.C. AlGaAs double-heterostructure diode lasers fabricated on a monolithic GaAs/Si substrate. *Appl. Phys. Lett.* **1984**, *45*, 309–311. [CrossRef]
74. Windhorn, T.H.; Metze, G.M. Room-temperature operation of GaAs/AlGaAs diode lasers fabricated on a monolithic GaAs/Si substrate. *Appl. Phys. Lett.* **1985**, *47*, 1031–1033. [CrossRef]
75. Fischer, R.; Kopp, W.; Morkoc, H.; Pion, M.; Specht, A.; Burkhart, G.; Appelman, H.; McGougan, D.; Rice, R. Low threshold laser operation at room temperature in GaAs/(Al, Ga) As structures grown directly on (100) Si. *Appl. Phys. Lett.* **1986**, *48*, 1360–1361. [CrossRef]
76. Razeghi, M.; Defour, M.; Omnes, F.; Maurel, P.; Chazelas, J.; Brillouet, F. First GaInAsP-InP double-heterostructure laser emitting at 1.27 um on a silicon substrate. *Appl. Phys. Lett.* **1988**, *53*, 725–727. [CrossRef]
77. Razeghi, M.; Defour, M.; Blondeau, R.; Omnes, F.; Maurel, P.; Acher, O.; Brillouet, F.; Fan, J.C.; Salerno, J. First cw op-eration of a Ga0.25In0.75As0.5P0.5-InP laser on a silicon substrate. *Appl. Phys. Lett.* **1988**, *53*, 2389–2390. [CrossRef]
78. Besancon, C.; Néel, D.; Make, D.; Ramírez, J.M.; Cerulo, G.; Vaissiere, N.; Decobert, J. AlGaInAs multi-quantum well lasers on silicon-on-insulator photonic integrated circuits based on InP-seed-bonding and epitaxial regrowth. *Appl. Sci.* **2021**, *12*, 263. [CrossRef]
79. Egawa, T.; Ogawa, A.; Jimbo, T.; Umeno, M. AlGaAs/GaAs laser diodes with GaAs islands active regions on Si grown by droplet epitaxy. *Jpn. J. Appl. Phys.* **1998**, *37*, 1552. [CrossRef]
80. Chen, S.; Li, W.; Wu, J.; Jiang, Q.; Tang, M.; Shutts, S.; Elliott, S.N.; Sobiesierski, A.; Seeds, A.J.; Ross, I.; et al. Electrically pumped continuous-wave III--V quantum dot lasers on silicon. *Nat. Photonics* **2016**, *10*, 307–311. [CrossRef]
81. Norman, J.; Kennedy, M.J.; Selvidge, J.; Li, Q.; Wan, Y.; Liu, A.Y.; Callahan, P.G.; Echlin, M.P.; Pollock, T.M.; Lau, K.M.; et al. Electrically pumped continuous wave quantum dot lasers epitaxially grown on patterned, on-axis (001) Si. *Opt. Express* **2017**, *25*, 3927–3934. [CrossRef]
82. Wei, W.-Q.; Feng, Q.; Guo, J.-J.; Guo, M.-C.; Wang, J.-H.; Wang, Z.-H.; Wang, T.; Zhang, J.-J. InAs/GaAs quantum dot nar-row ridge lasers epitaxially grown on SOI substrates for silicon photonic integration. *Opt. Express* **2020**, *28*, 26555–26563. [CrossRef] [PubMed]
83. Wan, Y.; Li, Q.; Liu, A.Y.; Gossard, A.C.; Bowers, J.E.; Hu, E.L.; Lau, K.M. Optically pumped 1.3 μm room-temperature InAs quantum-dot micro-disk lasers directly grown on (001) silicon. *Opt. Lett.* **2016**, *41*, 1664–1667. [CrossRef]
84. Wan, Y.; Li, Q.; Liu, A.Y.; Chow, W.W.; Gossard, A.C.; Bowers, J.E.; Hu, E.L.; Lau, K.M. Sub-wavelength InAs quantum dot micro-disk lasers epitaxially grown on exact Si (001) substrates. *Appl. Phys. Lett.* **2016**, *108*, 221101. [CrossRef]
85. Wan, Y.; Norman, J.; Li, Q.; Kennedy, M.J.; Liang, D.; Zhang, C.; Huang, D.; Zhang, Z.; Liu, A.Y.; Torres, A.; et al. 1.3 μm submilliamp threshold quantum dot micro-lasers on Si. *Optica* **2017**, *4*, 940–944. [CrossRef]
86. Jung, D.; Norman, J.; Kennedy, M.J.; Shang, C.; Shin, B.; Wan, Y.; Gossard, A.C.; Bowers, J.E. High efficiency low threshold current 1.3 μm InAs quantum dot lasers on on-axis (001) GaP/Si. *Appl. Phys. Lett.* **2017**, *111*, 122107. [CrossRef]
87. Kwoen, J.; Jang, B.; Watanabe, K.; Arakawa, Y. High-temperature continuous-wave operation of directly grown InAs/GaAs quantum dot lasers on on-axis Si (001). *Opt. Express* **2019**, *27*, 2681–2688. [CrossRef] [PubMed]
88. Wan, Y.; Zhang, S.; Norman, J.C.; Kennedy, M.J.; He, W.; Liu, S.; Xiang, C.; Shang, C.; He, J.-J.; Gossard, A.C.; et al. Tunable quantum dot lasers grown directly on silicon. *Optica* **2019**, *6*, 1394–1400. [CrossRef]
89. Wan, Y.; Zhang, S.; Norman, J.C.; Kennedy, M.; He, W.; Tong, Y.; Shang, C.; He, J.; Tsang, H.K.; Gossard, A.C.; et al. Directly modulated single-mode tunable quantum dot lasers at 1.3 μm. *Laser Photonics Rev.* **2020**, *14*, 1900348. [CrossRef]

90. Wan, Y.; Norman, J.C.; Tong, Y.; Kennedy, M.J.; He, W.; Selvidge, J.; Shang, C.; Dumont, M.; Malik, A.; Tsang, H.K.; et al. 1.3 μm quantum dot-distributed feedback lasers directly grown on (001) Si. *Laser Photonics Rev.* **2020**, *14*, 2000037. [CrossRef]
91. Wan, Y.; Shang, C.; Norman, J.; Shi, B.; Li, Q.; Collins, N.; Dumont, M.; Lau, K.M.; Gossard, A.C.; Bowers, J.E. Low threshold quantum dot lasers directly grown on unpatterned quasi-nominal (001) Si. *IEEE J. Sel. Top. Quantum Electron.* **2020**, *26*, 1–9. [CrossRef]
92. Shang, C.; Selvidge, J.; Hughes, E.; Norman, J.C.; Taylor, A.A.; Gossard, A.C.; Mukherjee, K.; Bowers, J.E. A Pathway to Thin GaAs Virtual Substrate on On-Axis Si (001) with Ultralow Threading Dislocation Density. *Phys. Status Solidi* **2021**, *218*, 2000402. [CrossRef]
93. Shang, C.; Hughes, E.; Wan, Y.; Dumont, M.; Koscica, R.; Selvidge, J.; Herrick, R.; Gossard, A.C.; Mukherjee, K.; Bowers, J.E. High-temperature reliable quantum-dot lasers on Si with misfit and threading dislocation filters. *Optica* **2021**, *8*, 749–754. [CrossRef]
94. Shang, C.; Feng, K.; Hughes, E.T.; Clark, A.; Debnath, M.; Koscica, R.; Leake, G.; Herman, J.; Harame, D.; Ludewig, P.; et al. Electrically pumped quantum-dot lasers grown on 300 mm patterned Si photonic wafers. *Light Sci. Appl.* **2022**, *11*, 299. [CrossRef] [PubMed]
95. Wei, W.-Q.; He, A.; Yang, B.; Wang, Z.-H.; Huang, J.-Z.; Han, D.; Ming, M.; Guo, X.; Su, Y.; Zhang, J.-J.; et al. Monolithic integration of embedded III-V lasers on SOI. *Light Sci. Appl.* **2023**, *12*, 84. [CrossRef]
96. Chen, J.J.; Wang, Z.H.; Wei, W.Q.; Wang, T.; Zhang, J.J. Sole excited-state InAs quantum dot laser on silicon with strong feedback resistance. *Front. Mater.* **2021**, *8*, 648049. [CrossRef]
97. Duan, J.; Huang, H.; Dong, B.; Norman, J.C.; Zhang, Z.; Bowers, J.E.; Grillot, F. Dynamic and nonlinear properties of epitaxial quantum dot lasers on silicon for isolator-free integration. *Photonics Res.* **2019**, *7*, 1222–1228. [CrossRef]
98. Feng, M.; Liu, J.; Sun, Q.; Yang, H. III-nitride semiconductor lasers grown on Si. *Prog. Quantum Electron.* **2021**, *77*, 100323. [CrossRef]
99. Arefin, R.; Ramachandra, S.H.; Jung, H.; You, W.; Hasan, S.M.N.; Turski, H.; Dwivedi, S.; Arafin, S. III-N/Si_3N_4 Integrated Photonics Platform for Blue Wavelengths. *IEEE J. Quantum Electron.* **2020**, *56*, 1–9. [CrossRef]
100. Siddharth, A.; Wunderer, T.; Lihachev, G.; Voloshin, A.S.; Haller, C.; Wang, R.N.; Teepe, M.; Yang, Z.; Liu, J.; Riemensberger, J.; et al. Near ultraviolet photonic integrated lasers based on silicon nitride. *APL Photonics* **2022**, *7*, 046108. [CrossRef]
101. Wunderer, T.; Siddharth, A.; Johnson, N.M.; Chua, C.L.; Teepe, M.; Yang, Z.; Batres, M.; Kippenberg, T.J. Low-noise hybrid photonic integrated violet and blue lasers for quantum applications. In Proceedings of the 2022 IEEE Research and Applications of Photonics in Defense Conference (RAPID), Miramar Beach, FL, USA, 12–14 September 2022; pp. 1–2. [CrossRef]
102. Wunderer, T.; Siddharth, A.; Johnson, N.M.; Chua, C.L.; Teepe, M.; Yang, Z.; Batres, M.; Maeda, P.; Lihachev, G.; Kippenberg, T.J. Single-frequency violet and blue laser emission from AlGaInN photonic integrated circuit chips. *Opt. Lett.* **2023**, *48*, 2781–2784. [CrossRef] [PubMed]
103. Koppens, F.H.L.; Mueller, T.; Avouris, P.; Ferrari, A.C.; Vitiello, M.S.; Polini, M. Photodetectors based on graphene, other two-dimensional materials and hybrid systems. *Nat. Nanotechnol.* **2014**, *9*, 780–793. [CrossRef] [PubMed]
104. Mu, C.; Xiang, J.; Liu, Z. Photodetectors based on sensitized two-dimensional transition metal dichalcogenides—A review. *J. Mater. Res.* **2017**, *32*, 4115–4131. [CrossRef]
105. Zhang, L.; Wang, B.; Zhou, Y.; Wang, C.; Chen, X.; Zhang, H. Synthesis Techniques, Optoelectronic Properties, and Broadband Photodetection of Thin-Film Black Phosphorus. *Adv. Opt. Mater.* **2020**, *8*, 2000045. [CrossRef]
106. Xia, F.; Wang, H.; Xiao, D.; Dubey, M.; Ramasubramaniam, A. Two-dimensional material nanophotonics. *Nat. Photonics* **2014**, *8*, 899–907. [CrossRef]
107. Lan, C.; Shi, Z.; Cao, R.; Li, C.; Zhang, H. 2D materials beyond graphene toward Si integrated infrared optoelectronic devices. *Nanoscale* **2020**, *12*, 11784–11807. [CrossRef] [PubMed]
108. Ugeda, M.M.; Bradley, A.J.; Shi, S.-F.; Da Jornada, F.H.; Zhang, Y.; Qiu, D.Y.; Ruan, W.; Mo, S.-K.; Hussain, Z.; Shen, Z.-X.; et al. Giant bandgap renormalization and excitonic effects in a monolayer transition metal dichalcogenide semiconductor. *Nat. Mater.* **2014**, *13*, 1091–1095. [CrossRef]
109. Ye, Y.; Wong, Z.J.; Lu, X.; Ni, X.; Zhu, H.; Chen, X.; Wang, Y.; Zhang, X. Monolayer excitonic laser. *Nat. Photonics* **2015**, *9*, 733–737. [CrossRef]
110. Amani, M.; Lien, D.-H.; Kiriya, D.; Xiao, J.; Azcatl, A.; Noh, J.; Madhvapathy, S.R.; Addou, R.; Kc, S.; Dubey, M.; et al. Near-unity photoluminescence quantum yield in MoS_2. *Science* **2015**, *350*, 1065–1068. [CrossRef]
111. Lee, Y.; Ghimire, G.; Roy, S.; Kim, Y.; Seo, C.; Sood, A.K.; Jang, J.I.; Kim, J. Impeding exciton—Exciton annihilation in monolayer WS2 by laser irradiation. *ACS Photonics* **2018**, *5*, 2904–2911. [CrossRef]
112. Danovich, M.; Zólyomi, V.; Aleiner, I.L.; Fal'ko, V.I. Auger recombination of dark excitons in WS2 and WSe2 monolayers. *2D Materials* **2016**, *3*, 035011. [CrossRef]
113. Wu, J.; Ma, H.; Yin, P.; Ge, Y.; Zhang, Y.; Li, L.; Zhang, H.; Lin, H. Two-dimensional materials for integrated photonics: Recent advances and future challenges. *Small Sci.* **2021**, *1*, 2000053. [CrossRef]
114. Li, Y.; Zhang, J.; Huang, D.; Sun, H.; Fan, F.; Feng, J.; Wang, Z.; Ning, C.-Z. Room-temperature continuous-wave lasing from monolayer molybdenum ditelluride integrated with a silicon nanobeam cavity. *Nat. Nanotechnol.* **2017**, *12*, 987–992. [CrossRef]
115. Fang, H.; Liu, J.; Li, H.; Zhou, L.; Liu, L.; Li, J.; Wang, X.; Krauss, T.F.; Wang, Y. 1305 nm few-layer MoTe2-on-silicon laser-like emission. *Laser Photonics Rev.* **2018**, *12*, 1800015. [CrossRef]

116. Liu, Y.; Fang, H.; Rasmita, A.; Zhou, Y.; Li, J.; Yu, T.; Xiong, Q.; Zheludev, N.; Liu, J.; Gao, W. Room temperature nanocavity laser with interlayer excitons in 2D heterostructures. *Sci. Adv.* **2019**, *5*, eaav4506. [CrossRef]
117. Salehzadeh, O.; Djavid, M.; Tran, N.H.; Shih, I.; Mi, Z. Optically pumped two-dimensional MoS2 lasers operating at room-temperature. *Nano Lett.* **2015**, *15*, 5302–5306. [CrossRef]
118. Reed, J.C.; Zhu, A.Y.; Zhu, H.; Yi, F.; Cubukcu, E. Wavelength tunable microdisk cavity light source with a chemically enhanced MoS2 emitter. *Nano Lett.* **2015**, *15*, 1967–1971. [CrossRef]
119. Duong, N.M.H.; Xu, Z.-Q.; Kianinia, M.; Su, R.; Liu, Z.; Kim, S.; Bradac, C.; Tran, T.T.; Wan, Y.; Li, L.-J.; et al. Enhanced emission from WSe2 monolayers coupled to circular Bragg gratings. *ACS Photonics* **2018**, *5*, 3950–3955. [CrossRef]
120. Liu, N.; Yang, X.; Zhang, J.; Zhu, Z.; Liu, K. Room-Temperature Excitonic Nanolaser Array with Directly Grown Monolayer WS2. *ACS Photonics* **2022**, *10*, 283–289. [CrossRef]
121. Jung, H.; Ahn, N.; Klimov, V.I. Prospects and challenges of colloidal quantum dot laser diodes. *Nat. Photonics* **2021**, *15*, 643–655. [CrossRef]
122. Efros, A.L.; Rosen, M. The electronic structure of semiconductor nanocrystals. *Annu. Rev. Mater. Sci.* **2000**, *30*, 475–521. [CrossRef]
123. Park, Y.-S.; Roh, J.; Diroll, B.T.; Schaller, R.D.; Klimov, V.I. Colloidal quantum dot lasers. *Nat. Rev. Mater.* **2021**, *6*, 382–401. [CrossRef]
124. Arakawa, Y.; Sakaki, H. Multidimensional quantum well laser and temperature dependence of its threshold current. *Appl. Phys. Lett.* **1982**, *40*, 939–941. [CrossRef]
125. Klimov, V.I.; Mikhailovsky, A.A.; Xu, S.; Malko, A.; Hollingsworth, J.A.; Leatherdale, C.A.; Eisler, H.-J.; Bawendi, M.G. Optical gain and stimulated emission in nanocrystal quantum dots. *Science* **2000**, *290*, 314–317. [CrossRef] [PubMed]
126. Fan, F.; Voznyy, O.; Sabatini, R.P.; Bicanic, K.T.; Adachi, M.M.; McBride, J.R.; Reid, K.R.; Park, Y.-S.; Li, X.; Jain, A.; et al. Continuous-wave lasing in colloidal quantum dot solids enabled by facet-selective epitaxy. *Nature* **2017**, *544*, 75–79. [CrossRef]
127. Taghipour, N.; Whitworth, G.L.; Othonos, A.; Dalmases, M.; Pradhan, S.; Wang, Y.; Kumar, G.; Konstantatos, G. Low-Threshold, Highly Stable Colloidal Quantum Dot Short-Wave Infrared Laser enabled by Suppression of Trap-Assisted Auger Recombination. *Adv. Mater.* **2022**, *34*, 2107532. [CrossRef]
128. Adachi, M.M.; Fan, F.; Sellan, D.P.; Hoogland, S.; Voznyy, O.; Houtepen, A.J.; Parrish, K.D.; Kanjanaboos, P.; Malen, J.A.; Sargent, E.H. Microsecond-sustained lasing from colloidal quantum dot solids. *Nat. Commun.* **2015**, *6*, 8694. [CrossRef] [PubMed]
129. Kozlov, O.V.; Park, Y.-S.; Roh, J.; Fedin, I.; Nakotte, T.; Klimov, V.I. Sub-single-exciton lasing using charged quantum dots coupled to a distributed feedback cavity. *Science* **2019**, *365*, 672–675. [CrossRef] [PubMed]
130. Roh, J.; Park, Y.-S.; Lim, J.; Klimov, V.I. Optically pumped colloidal-quantum-dot lasing in LED-like devices with an integrated optical cavity. *Nat. Commun.* **2020**, *11*, 271. [CrossRef] [PubMed]
131. Taghipour, N.; Dalmases, M.; Whitworth, G.L.; Dosil, M.; Othonos, A.; Christodoulou, S.; Liga, S.M.; Konstantatos, G. Colloidal Quantum Dot Infrared Lasers Featuring Sub-Single-Exciton Threshold and Very High Gain. *Adv. Mater.* **2023**, *35*, 2207678. [CrossRef] [PubMed]
132. Chang, H.; Min, K.; Lee, M.; Kang, M.; Park, Y.; Cho, K.-S.; Roh, Y.-G.; Hwang, S.W.; Jeon, H. Colloidal Quantum Dot Lasers Built on a Passive Two-Dimensional Photonic Crystal Backbone. *Nanoscale* **2016**, *8*, 6571–6576. [CrossRef]
133. Xie, W.; Stöferle, T.; Raino, G.; Aubert, T.; Bisschop, S.; Zhu, Y.; Mahrt, R.F.; Geiregat, P.; Brainis, E.; Hens, Z.; et al. On-Chip Integrated Quantum-Dot–Silicon-Nitride Microdisk Lasers. *Adv. Mater.* **2017**, *29*, 1604866. [CrossRef]
134. Lim, J.; Park, Y.-S.; Klimov, V.I. Optical gain in colloidal quantum dots achieved with direct-current electrical pumping. *Nat. Mater* **2018**, *17*, 42–49. [CrossRef]
135. Ahn, N.; Livache, C.; Pinchetti, V.; Jung, H.; Jin, H.; Hahm, D.; Park, Y.-S.; Klimov, V.I. Electrically Driven Amplified Spontaneous Emission from Colloidal Quantum Dots. *Nature* **2023**, *617*, 79–85. [CrossRef] [PubMed]